

An improved analysis of GW150914 using a fully spin-precessing waveform model

The LIGO Scientific Collaboration and The Virgo Collaboration

This paper presents updated estimates of source parameters for GW150914, a binary black-hole coalescence event detected by the Laser Interferometer Gravitational-wave Observatory (LIGO) on September 14, 2015 [1]. Reference [2] presented parameter estimation of the source using a 13-dimensional, phenomenological precessing-spin model (precessing IMRPhenom) and a 11-dimensional nonprecessing effective-one-body (EOB) model calibrated to numerical-relativity simulations, which forces spin alignment (nonprecessing EOBNR). Here we present new results that include a 15-dimensional precessing-spin waveform model (precessing EOBNR) developed within the EOB formalism. We find good agreement with the parameters estimated previously [2], and we quote updated component masses of $35_{-3}^{+5} M_{\odot}$ and $30_{-4}^{+3} M_{\odot}$ (where errors correspond to 90% symmetric credible intervals). We also present slightly tighter constraints on the dimensionless spin magnitudes of the two black holes, with a primary spin estimate < 0.65 and a secondary spin estimate < 0.75 at 90% probability. Reference [2] estimated the systematic parameter-extraction errors due to waveform-model uncertainty by combining the posterior probability densities of precessing IMRPhenom and nonprecessing EOBNR. Here we find that the two precessing-spin models are in closer agreement, suggesting that these systematic errors are smaller than previously quoted.

PACS numbers: 04.80.Nn, 04.25.dg, 95.85.Sz, 97.80.-d

I. INTRODUCTION

The detection of the first gravitational-wave (GW) transient, GW150914, by the Laser Interferometer Gravitational-wave Observatory (LIGO) on September 14, 2015 [1] marked the beginning of a new kind of astronomy, fundamentally different from electromagnetic or particle astronomy. GW150914 was analyzed using the most accurate signal models available at the time of observation, which were developed under the assumption that general relativity is the correct theory of gravity. The analysis concluded that GW150914 was generated by the coalescence of two black holes (BHs) of rest-frame masses $36_{-4}^{+5} M_{\odot}$ and $29_{-4}^{+4} M_{\odot}$, at a luminosity distance of 410_{-180}^{+160} Mpc [2]. Throughout this paper, we quote parameter estimates as the median of their posterior probability density, together with the width of the 90% symmetric credible interval.

The GW signal emitted by a binary black hole (BBH) depends on 15 independent parameters: the BH masses, the BH spin vectors, the line of sight to the detector (parametrized by two angles), the sky location of the binary (parametrized by two angles), the polarization angle of the GW, the luminosity distance of the binary, and the time of arrival of the GW at the detector. The task of extracting all 15 parameters from interferometric detector data relies on efficient Bayesian inference algorithms and on the availability of accurate theoretical predictions of the GW signal. State-of-the-art numerical-relativity (NR) simulations [3–8] can generate very accurate BBH waveforms over a large region of parameter space; however, this region does not yet include (i) binary configurations that have both large dimensionless spins (> 0.5), extreme mass ratios ($> 1/3$) and many GW cycles (≥ 40 –60), except for a few cases [8–10]; nor does it include (ii) systems undergoing significant spin-induced precession of the orbital plane. In practice, since

parameter estimation requires very many waveform evaluations that span a large region of the parameter space, a purely NR approach is unfeasible. Therefore, great effort has been devoted to building semi-analytical waveform models that are more efficient computationally than full-fledged NR, while still sufficiently accurate for the purposes of extracting unbiased physical information from the data.

The first parameter-estimation study of GW150914 [2] used two such models: an effective-one-body (EOB, [11, 12]) model that restricts spins to be aligned with the orbital angular momentum [13], and a phenomenological model that includes spin-precession effects governed by four effective spin parameters [14]. Here we present updated parameter estimates using a *fully spin-precessing* EOB model [15, 16], which is parametrized by the full set of BBH properties listed above, including all six BH-spin degrees of freedom, and which reflects additional physical effects described in Sec. II. The inclusion of these effects motivates us to repeat the Bayesian analysis of GW150914 with precessing EOB waveforms. This model was not used in Ref. [2] because it requires costly time-domain integration for each set of BBH parameters; thus, not enough Monte Carlo samples had yet been collected by the time the study was finalized.

The main result of our analysis is that the two precessing models (phenomenological and EOB) are broadly consistent, more so than the precessing phenomenological and nonprecessing EOB models compared in Ref. [2]. In that study, the parameter estimates obtained with those two models were combined with equal weights to provide the fiducial values quoted in Ref. [1], and they were differenced to characterize systematic errors due to waveform mismodeling. Because the two precessing models yield closer results, we are now able to report smaller combined credible intervals, as well as smaller estimated systematic errors. Nevertheless, the combined medians

cited as fiducial estimates in Ref. [1] change only slightly. In addition, we find that some of the *intrinsic* parameters that affect BBH evolution, such as the *in-plane* combination of BH spins that governs precession, are constrained better using the precessing EOB model.

Because precessing-EOB waveforms are so computationally expensive to generate, we cannot match the number of Monte Carlo samples used in Ref. [2]. Thus, we carry out a careful statistical analysis to assess the errors of our summary statistics (posterior medians and credible intervals) due to the finite number of samples. We apply the same analysis to the precessing phenomenological and nonprecessing EOB models, and to their combinations. Although finite-sample errors are a factor of a few larger for the precessing EOB model than for the other two, they remain much smaller than the credible intervals, so none of our conclusions are affected. Last, as a further test on the accuracy and consistency of the two precessing models, we use them to estimate the known parameters of a GW150914-like NR waveform injected into LIGO data. The resulting posteriors are similar to those found for GW150914.

This article is organized as follows. In Sec. II we discuss the modeling of spin effects in the BBH waveforms used in this paper. In Sec. III we describe our analysis. We present our results in Sec. IV, and our conclusions in Sec. V. Throughout the article we adopt geometrized units, with $G = c = 1$.

II. MODELING ORBITAL PRECESSION IN BBH WAVEFORM MODELS

Astrophysical stellar-mass BHs are known to possess significant intrinsic spins, which can engender large effects in the late phase of BBH coalescences: they affect the evolution of orbital frequency, and (if the BH spins are not aligned with the orbital angular momentum) they induce the precession of the orbital plane, modulating the fundamental chirping structure of emitted GWs in a manner dependent on the relative angular geometry of binary and observatory [17]. While measuring BH spins is interesting in its own right, the degree of their alignment and the resulting degree of precession hold precious clues to the astrophysical origin of stellar-mass BBHs [18]: aligned spins suggest that the two BHs were born from an undisturbed binary star in which both components successively collapsed to BHs; nonaligned spins point to an origin from capture events and three-body interactions in dense stellar environments.

Clearly, the accurate modeling of BH-spin effects is crucial to BBH parameter-estimation studies. Now, even state-of-the-art semianalytical waveform models still rely on a set of approximations that necessarily limit their accuracy. These include finite PN order, calibration to a limited number of NR simulations, rotation to precessing frames, and more. Thus, being able to compare parameter estimates performed with different waveform models,

derived under different assumptions and approximations (e.g., in time- vs. frequency-domain formulations), becomes desirable to assess the systematic biases due to waveform mismodeling. While observing consistent results does not guarantee the absence of systematics (after all, multiple models could be wrong in the same way), the fact that we do not observe inconsistencies does increase our confidence in the models.

Such a comparison was performed in the original parameter-estimation study of GW150914 [2], showing consistency between the precessing phenomenological model and the aligned-spin EOBNR model. This result matched the finding that the BH spins were approximately aligned in GW150914, or that precession effects were too weak to be detected, because of the small number of GW cycles and of the (putative) face-on/face-off presentation of the binary. Nevertheless, it may be argued that the conclusion of consistency remained suspect, because only one model in the analysis carried information about the effects of precession; conversely, the estimates of mismodeling systematics performed in Ref. [2] were likely increased by the fact that the nonprecessing model would be biased by what little precession may be present in the signal.

The analysis presented in this article, which relies on two precessing-spin waveform families, removes both limitations, and sets up a more robust framework to assess systematic biases in future detections where spin effects play a larger role. In the rest of this section, we discuss the features and formulation of the fully precessing EOBNR model. The reader not interested in these technical details (and in the Bayesian-inference setup of Sec. III) may proceed directly to Sec. IV.

The precessing EOBNR model (henceforth, “precessing EOBNR”) used here describes inspiral–merger–ringdown (IMR) waveforms for coalescing, quasicircular BH binaries with mass ratio $0.01 \leq q \equiv m_2/m_1 \leq 1$, dimensionless BH spin magnitudes $0 \leq \chi_{1,2} \equiv |\mathbf{S}_{1,2}|/m_{1,2}^2 \leq 0.99$, and arbitrary BH spin orientations.¹ We denote with $m_{1,2}$ the masses of the component objects in the binary, and with $\mathbf{S}_{1,2}$ their spin vectors.

The fundamental idea of EOB models consists in mapping the conservative dynamics of a binary to that of a spinning particle that moves in a deformed Kerr spacetime [11, 12, 19–24], where the magnitude of the deformation is proportional to the mass ratio of the binary. This mapping can be seen as a resummation of post-Newtonian (PN) formulas [25] with the aim of extending their validity to the strong-field regime. As for dissipative effects, EOB models equate the loss of energy to the GW luminosity, which is expressed as a sum of squared amplitudes of the multipolar waveform modes. In the nonprecessing limit, the inspiral–plunge waveform modes

¹ In LIGO Algorithm Library (LAL), as well as in technical publications, the precessing EOBNR model that we use is called SEOBNRv3.

are themselves resummations of PN expressions [26–28], and are functionals of the orbital dynamics. The ringdown signal is described by a linear superposition of the quasinormal modes [29–31] of the remnant BH.

EOB models can be tuned to NR by introducing adjustable parameters at high, unknown PN orders. For the precessing EOB model used in this work, the relevant calibration to NR was carried out in Ref. [13] against 38 NR simulations of nonprecessing-spins systems from Ref. [32], with mass ratios up to 1/8 and spin magnitudes up to almost extremal for equal-mass BBHs and up to 0.5 for unequal-mass BBHs.

Furthermore, information from inspiral, merger and ringdown waveforms in the test-particle limit were also included in the EOBNR model [33, 34]. Prescriptions for the onset and spectrum of ringdown for precessing BBHs were first given in Ref. [15], and significantly improved in Ref. [16].

In the model, the BH spin vectors precess according to

$$\frac{d\mathbf{S}_{1,2}}{dt} = \frac{\partial H_{\text{EOB}}}{\partial \mathbf{S}_{1,2}} \times \mathbf{S}_{1,2}; \quad (1)$$

when the BH spins are oriented generically, the orbital plane precesses with respect to an inertial observer. The orientation of the orbital plane is tracked by the Newtonian orbital angular momentum $\mathbf{L}_N \equiv \mu \mathbf{r} \times \dot{\mathbf{r}}$, where $\mu \equiv m_1 m_2 / (m_1 + m_2)$ and \mathbf{r} is the relative BH separation. One defines a (noninertial) precessing frame whose z -axis is aligned with $\mathbf{L}_N(t)$, and whose x - and y -axes obey the minimum-rotation prescription of Ref. [35, 36]. In this frame, the waveform amplitude and phase modulations induced by precession are minimized, as pointed out in several studies [35–39].

Thus, the construction of a precessing EOB waveform consists of the following steps: (i) compute orbital dynamics numerically, by solving Hamilton’s equation for the EOB Hamiltonian, subject to energy loss, up until the light ring (or photon orbit) crossing; (ii) generate inspiral–plunge waveforms in the precessing frame as if the system were not precessing [13]; (iii) rotate the waveforms to the inertial frame aligned with the direction of the remnant spin; (iv) generate the ringdown signal, and connect it smoothly to the inspiral–plunge signal; (v) rotate the waveforms to the inertial frame of the observer.

A phenomenological precessing-spins IMR model (henceforth, “precessing IMRPhenom”) was proposed in Refs. [40, 41].² These waveforms are generated in the frequency domain by rotating nonprecessing phenomenological waveforms [42] from a precessing frame to the inertial frame of the observer, according to PN formulas that describe precession in terms of Euler angles. The underlying nonprecessing waveforms depend on the BH masses and on the two projections of the spins on the Newtonian angular momentum, with the spin of the BH

formed through merger adjusted to also take into account the effect of the in-plane spin components. The influence of the in-plane spin components on the precession is modeled with a single spin parameter (a function of the two BH spins), and depends also on the initial phase of the binary in the orbital plane. Thus, this model has only four independent parameters to describe the six spin degrees of freedom, which is justified by the analysis of dominant spin effects performed in Ref. [40].

While both precessing EOBNR and IMRPhenom models describe spin effects, there are important differences in how they account for precession, which is the main focus of this paper.

1. In precessing IMRPhenom, the precessing-frame inspiral–plunge waveforms are strictly nonprecessing waveforms, while for precessing EOBNR some precessional effects are included (such as spin–spin frequency and amplitude modulations), since the orbital dynamics that enters the nonprecessing expressions for the GW modes is fully precessing.
2. The precessing EOBNR merger–ringdown signal is generated in the inertial frame oriented along the total angular momentum of the remnant—the very frame where quasinormal mode frequencies are computed in BH perturbation theory. By contrast, precessing IMRPhenom generates the merger–ringdown signal directly in the precessing frame.
3. The IMRPhenom precessing-frame waveforms contain only the dominant $(2, \pm 2)$ modes, while precessing EOBNR includes also $(2, \pm 1)$ modes in the precessing frame, although these are not calibrated to NR.
4. In IMRPhenom, the frequency-domain rotation of the GW modes from the precessing frame to the inertial frame is based on approximate formulas (i.e., on the stationary-phase approximation), while precessing EOBNR computes the rotations fully in the time domain, where the formulas are straightforward.
5. In precessing IMRPhenom, the frequency-domain formulas for the Euler angles that parametrize the precession of the orbital plane with respect to a fixed inertial frame involve several approximations: in-plane spin components are orbit averaged; the magnitude of the orbital angular momentum is approximated by its 2PN nonspinning expression; the evolution of frequency is approximated as adiabatic; and the PN formulas that regulate the behavior of the Euler angles at high frequencies are resummed partially. By contrast, precessing EOBNR defines these Euler angles on the basis of the completely general motion of $\mathbf{L}_N(t)$; this motion is a direct consequence of the EOB dynamics, and as such it is sensitive to the full precessional dynamics of the six spin components.

² In LAL this precessing model is called IMRPhenomPv2.

A priori, it is not obvious that these approximations will not impact parameter estimation for a generic BBH. However, as far as GW150914 is concerned, Ref. [2] showed broadly consistent results between a precessing and a nonprecessing model; *a fortiori* we should expect similar results between two precessing models. Indeed, the GW150914 binary is most likely face-off or face-on with respect to the line of sight to the detector, and the component masses are almost equal [2]: both conditions imply that subdominant modes play a minor role.

The nonprecessing models that underlie both approximations were tested against a large catalog of NR simulations [13, 42, 43], finding a high degree of accuracy in the GW150914 parameter region. However, it is important to bare in mind that these waveform models can differ from NR outside the region in which they were calibrated and they do not account for all possible physical effects that are relevant to generic BBHs, such as higher-order modes. Finally, neither of the two precessing models has been calibrated to any precessing NR simulation. Thus, we cannot exclude that current precessing models are affected by systematics.

Since the generation of precessing EOBNR waveforms (at least in the current implementation in LAL) is a rather time-consuming process,³ when carrying out parameter-estimation studies with this template family, we introduce a time-saving approximation at the level of the likelihood function. Namely, we marginalize over the arrival time and phase of the signal as if the waveforms contained only $(2, \pm 2)$ inertial-frame modes, since in that case the marginalization can be performed analytically. We have determined that the impact of this approximation is negligible by conducting a partial parameter-estimation study where we do not marginalize over the arrival time and phase. We can understand this physically for GW150914 because in a nearly face-on/face-off binary the $(2, \pm 1)$ observer-frame modes are significantly sub-dominant compared to $(2, \pm 2)$ modes.⁴

III. BAYESIAN INFERENCE ANALYSIS

For each waveform model under consideration, we estimate the posterior probability density [44, 45] for the BBH parameters, following the prescriptions of Ref. [2]. To wit, we use the LAL implementation of parallel-tempering Markov Chain Monte Carlo and

nested sampling [46] to sample the posterior density $p(\boldsymbol{\vartheta}|\text{model, data})$ as a function of the parameter vector $\boldsymbol{\vartheta}$:

$$p(\boldsymbol{\vartheta}|\text{model, data}) \propto \mathcal{L}(\text{data}|\boldsymbol{\vartheta}) \times p(\boldsymbol{\vartheta}). \quad (2)$$

To obtain the likelihood $\mathcal{L}(\text{data}|\boldsymbol{\vartheta})$, we first generate the GW polarizations $h_+(\boldsymbol{\vartheta}_{\text{intrinsic}})$ and $h_\times(\boldsymbol{\vartheta}_{\text{intrinsic}})$ according to the waveform model. We then combine the polarizations into the LIGO detector responses $h_{1,2}$ by way of the detector antenna patterns:

$$h_k(\boldsymbol{\vartheta}) = h_+(\boldsymbol{\vartheta}_{\text{intrinsic}}) F_k^{(+)}(\boldsymbol{\vartheta}_{\text{extrinsic}}) + h_\times(\boldsymbol{\vartheta}_{\text{intrinsic}}) F_k^{(\times)}(\boldsymbol{\vartheta}_{\text{extrinsic}}). \quad (3)$$

Finally, we compute the likelihood as the sampling distribution of the residuals (i.e., the detector data d_k minus the GW response $h_k(\boldsymbol{\vartheta})$), under the assumption that these are distributed as Gaussian noise characterized by the power spectral density (PSD) of nearby data [46]:

$$\mathcal{L}(\text{data}|\boldsymbol{\vartheta}) \propto \exp \left[-\frac{1}{2} \sum_{k=1,2} \langle h_k(\boldsymbol{\vartheta}) - d_k | h_k(\boldsymbol{\vartheta}) - d_k \rangle \right], \quad (4)$$

where $\langle \cdot | \cdot \rangle$ denotes the noise-weighted inner product [47].

The prior probability density $p(\boldsymbol{\vartheta})$ follows the choices of Ref. [2]. In particular, we assume uniform mass priors $m_{1,2} \in [10, 80] M_\odot$, with the constraint $m_2 \leq m_1$, and uniform spin-amplitude priors $a_{1,2} = |\mathbf{S}_{1,2}|/m_{1,2}^2 \in [0, 1]$, with spin directions distributed uniformly on the two-sphere; and we assume that sources are distributed uniformly in Euclidian volume, with their orbital orientation distributed uniformly on the two-sphere. All the binary parameters that evolve during the inspiral (such as *tilt* angles between the spins and the orbital angular momentum, $\theta_{LS_{1,2}}$) are defined at a reference GW frequency $f_{\text{ref}} = 20$ Hz.

Following [2], we marginalize over the uncertainty in the calibration of LIGO data [48]. This broadens the posteriors but reduces calibration biases. For the precessing EOBNR analysis, we also marginalize over the time of arrival and reference phase of the GW signal, following the prescription of Ref. [49].

To assess whether the data is *informative* with regard to a source parameter (i.e., where it *updates* the prior significantly), we perform a Kolmogorov–Smirnov (KS) test. Given an empirical distribution (in our case, the Monte Carlo posterior samples) and a probability distribution (in our case, the prior), the KS test measures the maximum deviation between the two cumulative distributions and associates a p -value to that: for samples generated from the probability distribution against which the test is performed, one expects a p -value around 0.5; p -values smaller than 0.05 indicate that the samples come from a different probability distribution with a high level of significance. The outcomes of our KS tests are only statements about how much the posteriors deviate from the respective priors, but they do not tell us anything about the astrophysical relevance of 90% credible intervals.

³ Generating a nonspinning, equal-mass binary black-hole waveform for a total mass of $70 M_\odot$ from a starting frequency of 20 Hz is about a factor of 20 slower for precessing EOBNR than for precessing IMRPhenom.

⁴ By construction, the precessing IMRPhenom inertial-frame polarizations $h_{+, \times}$ depend on the arrival time and phase exactly as they would in a model that includes only $(2, \pm 2)$ inertial-frame modes. Thus, although precessing IMRPhenom does include $(2, \pm 1)$ inertial-frame modes, the analytical marginalization that we just discussed is exact.

IV. RESULTS

The first question that we address is whether parameter estimates performed using the two precessing models (precessing IMRPhenom and precessing EOBNR) are compatible. In particular, we wish to compare medians and 90% credible intervals (the summary statistics used in Ref. [2]) for the parameters tabulated in Table I of Ref. [2], as well as additional spin parameters. The nominal values of the medians and 5% and 95% quantiles for the two models are listed in the “EOBNR” and “IMRPhenom” columns of Table I. However, it is unclear *a priori* whether any differences are due to the models themselves, or to the imperfect sampling of the posteriors in Markov Chain Monte Carlo runs. This is a concern especially for the precessing EOBNR results, since the slower speed of EOBNR waveform generation means that shorter chains are available for parameter estimation. To gain trust in our comparisons, we characterize the Monte Carlo error of the medians and quantiles by a bootstrap analysis, as follows.

The Monte Carlo runs for the precessing IMRPhenom model produced an equal-weight posterior sampling consisting of 27,000 approximately independent samples, obtained by downsampling the original MCMC run by a factor equal to the largest autocorrelation length measured for the parameters of interest (those of Table I). We generate 1,000 Bayesian-bootstrap weighted resamplings [50] of the equal-weight population,⁵ and for each we compute the weighted medians and quantiles. We characterize the Monte Carlo error of these summary statistics as the 90% symmetric interquantile interval across the 1,000 realizations. For completeness, we apply the same analysis to the 45,000 samples of the nonprecessing EOBNR that were employed in Ref. [2].

The Monte Carlo runs for the precessing EOBNR model produced a sampling of 2,700 approximately independent samples, obtained by selecting every 11th sample in the original MCMC run. Again we generate 1,000 Bayesian-bootstrap resamplings, compute summary statistics on each, and measure their variation. However, to improve the representativeness of this analysis given the smaller number of samples in play, we use 9 additional equal-weight populations, obtained by selecting every $(11 + i)$ -th sample in the original MCMC run, for $i = 1, \dots, 9$. For each of the 1,000 Bayesian-bootstrap resamplings, we first choose randomly among the 10 equal-weight populations.

Monte Carlo errors are expected to shrink as the inverse square root of the number of samples; this is indeed what we observe, with precessing EOBNR finite-sample errors $\sim (27,000/2,700)^{1/2} \approx 3$ times larger than for precessing IMRPhenom. Table I and Figure 1 present the

results of this study for several key physical parameters of the source of GW150914. We display with darker colors the finite-sample error estimates on the position of the medians and 5% and 95% quantiles. Lighter colors represent the 90% credible intervals.

Combined estimates. To account for waveform-mismodeling errors in its fiducial parameter estimates, Ref. [2] cited quantiles for combined posteriors obtained by averaging the posteriors for its two models (in Bayesian terms, this corresponds to assuming that the observed GW signal could have come from either model with equal prior probability). We repeat the same procedure for the two precessing models, and we show the resulting estimates in the column “Overall” of Table I. Quantiles are more uncertain for the precessing combination due to the larger finite-sampling error of precessing EOBNR. Nevertheless, 90% credible intervals are slightly tighter than cited in Ref. [2]. In the Appendix, we provide a graphical representation of the combined estimates.

Posterior histograms: masses and spin magnitudes. We now discuss in some detail the salient features of parameter posteriors. In Figs. 2–6, we show the one-dimensional marginalized posteriors for selected pairs of parameters and 90% credible intervals (the dashed lines), as obtained for the two precessing models, as well as the two-dimensional probability density plots for the precessing EOBNR model. In Fig. 2, we show the posteriors for the *source-frame* BH masses $m_{1,2}$: these are measured fairly well, with statistical uncertainties around 10%. In Fig. 3, we show the posteriors for the dimensionless spin magnitudes $a_{1,2}$: the bound on a_1 is about 20% more stringent for precessing EOBNR. This is true even if we account for the larger finite-sampling uncertainty in the precessing EOBNR quantiles (see Table 1). The final spin presented in Table I and Figure 1 was obtained including the contribution from the in-plane spin components to the final spin [51]; previous publications [1, 2] just use the contribution from the aligned components of the spins, which remains sufficient for the final mass computation. Just using the aligned components does not change the precessing EOBNR result, but gives a precessing IMRPhenom result of $0.66^{+0.04}_{-0.06}$.

Posterior histograms: spin directions. Figure 4 reproduces the disk plot of Ref. [2] for precessing EOBNR. In this plot, the three-dimensional histograms of the dimensionless spin vectors $\mathcal{S}_{1,2}/m_{1,2}^2$ are projected onto a plane perpendicular to the orbital plane; the bins are designed so that each contains the same prior probability mass (i.e., histogramming the prior would result in a uniform shading). It is apparent that the data disfavor large spins aligned or antialigned with the orbital angular momentum, consistently with precessing IMRPhenom results. Because precessing EOBNR favors smaller values of the dimensionless spin magnitudes, the plot is darker toward its center than its counterpart in Ref. [2]. In agreement with that paper, our analysis does not support strong statements on the orientation of the BH spins with respect to the orbital angular mo-

⁵ For n samples, this involves generating 1,000 realizations of weights according to the $(n - 1)$ -variate Dirichlet distribution.

TABLE I. Median values of source parameters of GW150914 as estimated with the two precessing waveform models, and with an equal-weight average of posteriors (in the ‘‘Overall’’ column). The models are described in the text. Subscripts and superscripts indicate the range of the symmetric 90% credible intervals. When useful, we quote 90% credible bounds.

	precessing EOBNR	precessing IMRPhenom	Overall
Detector-frame total mass M/M_\odot	$71.6^{+4.3}_{-4.1}$	$70.9^{+4.0}_{-3.9}$	$71.3^{+4.3}_{-4.1}$
Detector-frame chirp mass \mathcal{M}/M_\odot	$30.9^{+2.0}_{-1.9}$	$30.6^{+1.8}_{-1.8}$	$30.8^{+1.9}_{-1.8}$
Detector-frame primary mass m_1/M_\odot	$38.9^{+5.1}_{-3.7}$	$38.5^{+5.6}_{-3.6}$	$38.7^{+5.3}_{-3.7}$
Detector-frame secondary mass m_2/M_\odot	$32.7^{+3.6}_{-4.8}$	$32.2^{+3.6}_{-4.8}$	$32.5^{+3.7}_{-4.8}$
Detector-frame final mass M_f/M_\odot	$68.3^{+3.8}_{-3.7}$	$67.6^{+3.6}_{-3.5}$	$68.0^{+3.8}_{-3.6}$
Source-frame total mass $M^{\text{source}}/M_\odot$	$65.6^{+4.1}_{-3.8}$	$65.0^{+4.0}_{-3.6}$	$65.3^{+4.1}_{-3.7}$
Source-frame chirp mass $\mathcal{M}^{\text{source}}/M_\odot$	$28.3^{+1.8}_{-1.7}$	$28.1^{+1.7}_{-1.6}$	$28.2^{+1.8}_{-1.7}$
Source-frame primary mass $m_1^{\text{source}}/M_\odot$	$35.6^{+4.8}_{-3.4}$	$35.3^{+5.2}_{-3.4}$	$35.4^{+5.0}_{-3.4}$
Source-frame secondary mass $m_2^{\text{source}}/M_\odot$	$30.0^{+3.3}_{-4.4}$	$29.6^{+3.3}_{-4.3}$	$29.8^{+3.3}_{-4.3}$
Source-frame final mass $M_f^{\text{source}}/M_\odot$	$62.5^{+3.7}_{-3.4}$	$62.0^{+3.7}_{-3.3}$	$62.2^{+3.7}_{-3.4}$
Mass ratio q	$0.84^{+0.14}_{-0.20}$	$0.84^{+0.14}_{-0.20}$	$0.84^{+0.14}_{-0.20}$
Effective inspiral spin parameter χ_{eff}	$-0.02^{+0.14}_{-0.16}$	$-0.05^{+0.13}_{-0.15}$	$-0.04^{+0.14}_{-0.16}$
Effective precession spin parameter χ_p	$0.28^{+0.38}_{-0.21}$	$0.35^{+0.45}_{-0.27}$	$0.31^{+0.44}_{-0.23}$
Dimensionless primary spin magnitude a_1	$0.22^{+0.43}_{-0.20}$	$0.32^{+0.53}_{-0.29}$	$0.26^{+0.52}_{-0.24}$
Dimensionless secondary spin magnitude a_2	$0.29^{+0.52}_{-0.27}$	$0.34^{+0.54}_{-0.31}$	$0.32^{+0.54}_{-0.29}$
Final spin a_f	$0.68^{+0.05}_{-0.05}$	$0.68^{+0.06}_{-0.06}$	$0.68^{+0.05}_{-0.06}$
Luminosity distance D_L/Mpc	440^{+160}_{-180}	440^{+150}_{-180}	440^{+160}_{-180}
Source redshift z	$0.094^{+0.032}_{-0.037}$	$0.093^{+0.029}_{-0.036}$	$0.093^{+0.030}_{-0.036}$
Upper bound on primary spin magnitude a_1	0.54	0.74	0.65
Upper bound on secondary spin magnitude a_2	0.70	0.78	0.75
Lower bound on mass ratio q	0.69	0.68	0.68

mentum. The spin opening angles (the *tilts*), defined by $\cos(\theta_{LS_{1,2}}) = (\mathbf{S}_{1,2} \cdot \hat{\mathbf{L}}_N) / |\mathbf{S}_{1,2}|$, are distributed broadly. However, the KS test described at the end of Sec. III does indicate some deviation between priors and posteriors, with p -values much smaller than 0.05 for $\cos(\theta_{LS_1})$ and $\cos(\theta_{LS_2})$.

Posterior histograms: effective spin parameters. In Fig. 5, we show the posteriors of the effective spin combinations χ_{eff} [19, 52–54] and χ_p [40] defined by

$$\chi_{\text{eff}} = \frac{c}{G} \left(\frac{\mathbf{S}_1}{m_1} + \frac{\mathbf{S}_2}{m_2} \right) \cdot \frac{\hat{\mathbf{L}}_N}{M}, \quad (5)$$

$$\chi_p = \frac{c}{B_1 G m_1^2} \max(B_1 S_{1\perp}, B_2 S_{2\perp}), \quad (6)$$

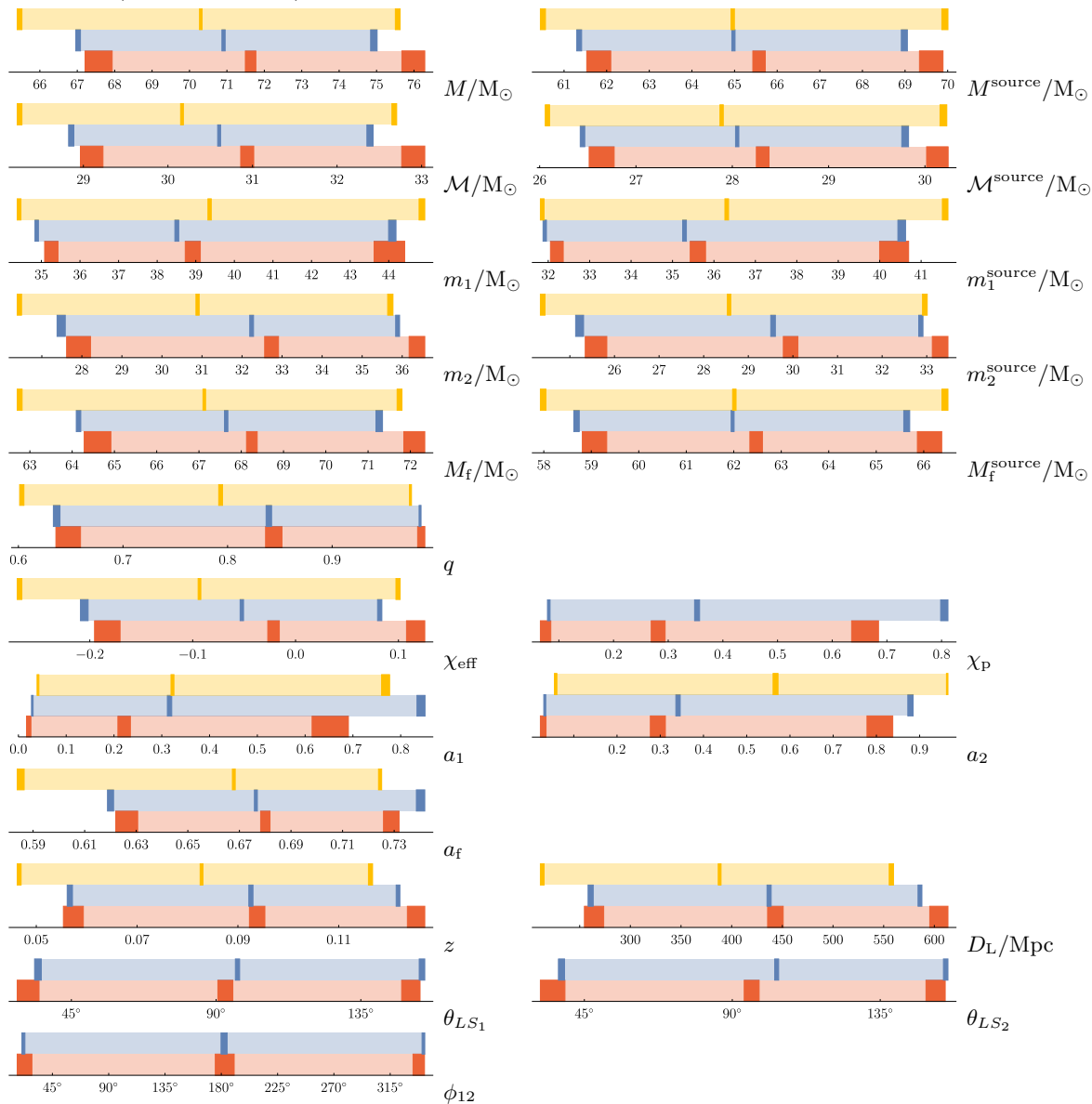
where $\mathbf{S}_{i\perp}$ is the component of the spin perpendicular to the orbital angular momentum \mathbf{L}_N , M is the total observed mass, $B_1 = 2 + 3q/2$ and $B_2 = 2 + 3/(2q)$, and $i = \{1, 2\}$.

While χ_{eff} combines the projections of the BH spins onto the orbital angular momentum, χ_p depends on their in-plane components, and thus relates to precessional effects. Both models have credible intervals for χ_{eff} that

contain the value 0, and deviate from the prior significantly. The data provides little information about precession, but show a slightly stronger preference for lower values of χ_p than expressed by our priors; the deviation is more pronounced for precessing EOBNR. The 90% credible intervals contain the value 0, and extend up to about 0.7 and 0.8 for precessing EOBNR and precessing IMRPhenom, respectively. Thus, precessing EOBNR provides a tighter upper bound.

Posterior histograms: other spin angles. To explore other possible differences between the two precessing models, we now consider spin parameters that were not reported in Ref. [2]. In particular, we compute posteriors for θ_{12} , the opening angle between the spin vectors, and ϕ_{12} , the opening angle between the in-plane projections of the spins. The prior on $\cos\theta_{12}$ is uniform in $[-1, 1]$, while the prior on ϕ_{12} is uniform in $[0, 2\pi]$. We show these posteriors in Fig. 6. The θ_{12} posteriors deviate appreciably from the prior, and are rather similar. By contrast, comparing the opening angle between spin projections onto orbital plane, ϕ_{12} , we find that the precessing EOBNR posterior deviates significantly from the prior (with KS p -value $\in [0.0077, 0.075]$), while the pre-

FIG. 1. Comparing nonprecessing EOBNR (light yellow, top), precessing IMRPhenom (light blue, middle), and precessing EOBNR (light red, bottom) 90% credible intervals for select GW150914 source parameters. The darker intervals represent error estimates for (from left to right) the 5%, 50% and 95% quantiles, estimated by Bayesian bootstrapping.



cessing IMRPhenom posterior does not (with KS p -value $\in [0.30, 0.60]$). This is as it should be, since in precessing IMRPhenom binaries with identical projection of the total spin on the orbital plane have identical waveforms. Although the KS p -values suggest that the data provide information about θ_{12} and ϕ_{12} beyond the prior, we note that the 90% confidence intervals for both of these parameters cover approximately 90% of their valid ranges, and are indistinguishable for each waveform model.

Spin evolution All the source parameters discussed above are measured at a reference frequency of 20 Hz. Exploiting the capability of precessing EOBNR of evolving the BH spin vectors in the time domain, we may address the question of estimating values for the spin

parameters at the time of the merger. To do so, we randomly sample 1,000 distinct configurations from the precessing EOBNR posteriors, and we evolve them to the maximum EOB orbital frequency (a proxy for the merger in the model). We then produce histograms of the evolved values of χ_{eff} and χ_{p} . We find little if any change between 20 Hz and the merger. Indeed, a KS test suggests that the original and evolved distributions are very consistent, with p -values close to 1.

Comparison with numerical relativity The precessing EOBNR waveform model has been tested against numerical relativity (NR) waveforms using simulations from the SXS catalog [15, 16, 32]. We can provide a targeted cross-check on the accuracy of precessing

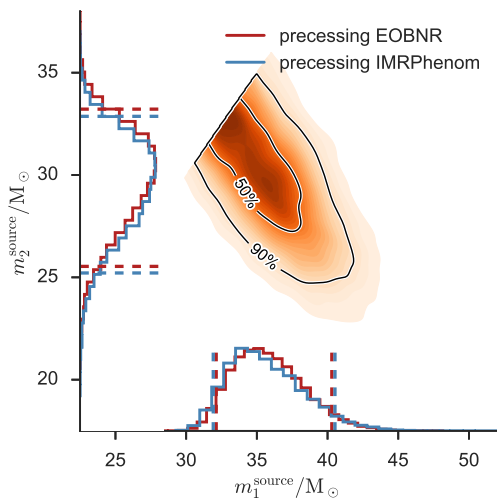


FIG. 2. Posterior probability densities for the source-frame component masses m_1^{source} and m_2^{source} , where $m_2^{\text{source}} \leq m_1^{\text{source}}$. We show one-dimensional histograms for precessing EOBNR (red) and precessing IMRPhenom (blue); the dashed vertical lines mark the 90% credible intervals. The two-dimensional density plot shows 50% and 90% credible regions plotted over a color-coded posterior density function.

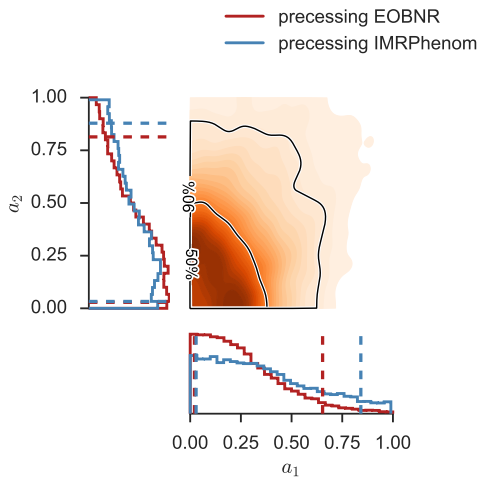


FIG. 3. Posterior probability densities for the dimensionless spin magnitudes. (See Fig. 2 for details.)

EOBNR near GW150914 by performing parameter estimation runs on mock NR signals injected into LIGO data. This test is complementary to an ongoing study of the same nature that however does not employ the precessing EOBNR model used in this paper. We use a new LAL infrastructure [55, 56] to inject spline-interpolated and tapered NR waveforms into detector data; spins are defined with respect to the orbital angular momentum at a reference frequency of 20 Hz. All higher harmonics of the GW signal are included up to the $l = 8$ multipole. At the inclinations used in this study the im-

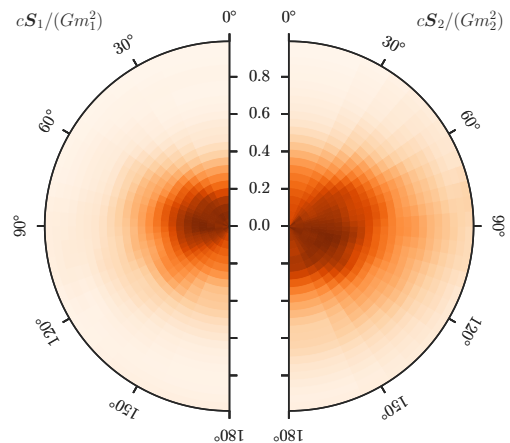


FIG. 4. Posterior probability density of BH spin directions, plotted as in Fig. 5 of Ref. [2].

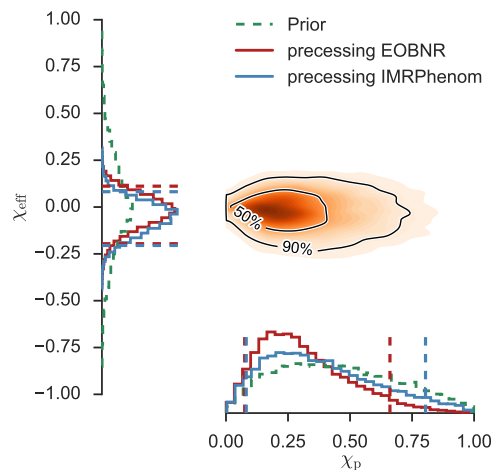


FIG. 5. Posterior probability densities of the effective spin and perpendicular effective spin. (See Fig. 2 for details.)

part of modes with $l > 2$ is small, but merits further study, a detailed analysis will be presented in a forthcoming paper. We restrict this investigation to a NR waveform which was computed by the SXS collaboration using the SpEC [57] code and is available in the public waveform catalogue [58] as SXS:BBH:0308. The intrinsic parameters of the NR waveform $q = 0.81$, $a_1 = 0.34$, and $a_2 = 0.67$ are consistent with the results obtained in Ref. [2] and this waveform agrees well with the detector data.

We can freely choose the angle between the line of sight and the angular momentum of the binary for mock NR signals. Since there is some uncertainty in the binary's inclination, we perform one run near maximum a posteriori probability (MaP) inclination, $\iota = 2.856$ rad (163.6°), and a second one at the upper bound of the 90% credible interval of the marginal probability density function (PDF) of the inclination, $\iota = 1.2$ rad (68.8°).

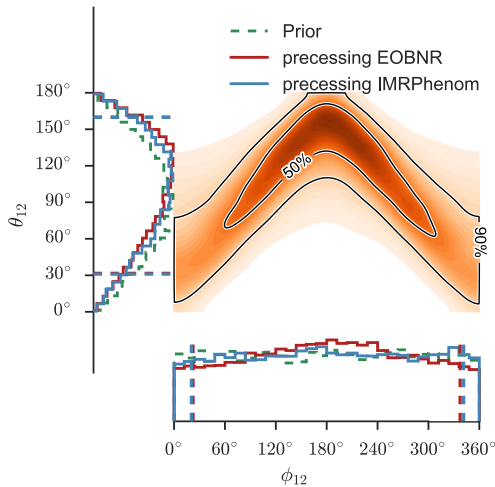


FIG. 6. Posterior probability densities of the opening angle between the two spins, θ_{12} , and the angle between the in-plane projections of the spins, ϕ_{12} . (See Fig. 2 for details.)

In Fig. 7 we show the two GW polarizations for the NR waveform and the precessing EOBNR model. The spin magnitudes and the mass ratio were fixed to the NR values. The directions of spins are defined to be the same at initial time: tilt angles are 18.8° , 149.4° , and the azimuthal angles, defined with respect to the initial separation vector, are 30.9° , 38.7° for the primary and secondary BHs, respectively. To quantify the agreement between those waveforms we compute overlaps averaged over the GW polarization and source sky location, which takes into account the uncertainty in those parameters. The polarization-sky-averaged overlap for MaP inclination is 0.997, and for $\iota = 1.2$ rad (68.8°) overlap is 0.993.

We show results for the run with MaP inclination for the source-frame component masses and effective spins in the left and right panels of Fig. 8. The precessing EOBNR and precessing IMRPhenom model show good agreement in the masses and effective precession spin χ_p . The posterior PDFs obtained for the effective aligned spin χ_{eff} are slightly offset. All injected values are found within the 90% credible regions. Results for the inclination chosen at the upper bound of the 90% credible interval of the marginal PDF of the inclination are qualitatively similar to the MaP results, except for the PDF of the effective precession spin which peaks around $\chi_p \sim 0.4$, noticeably above the injected value, but still well inside the 90% credible interval.

V. CONCLUSIONS

We presented an updated analysis of GW150914 with mass estimates of $35_{-3}^{+5} M_\odot$ and $30_{-4}^{+3} M_\odot$, and we refined parameter estimates using a generalized, fully precessing waveform model which depends on the full 15 independent parameters of a coalescing binary in circular orbit.

We find this analysis to be broadly consistent with the results in Ref. [2]. By using the difference between two precessing waveform models as a proxy for systematic errors due to waveform uncertainty, we can compute a more accurate systematic error than what was possible in Ref. [2]. By looking at differences in 5% and 95% quantiles between different waveform models in Fig. 1, one can observe, on average, more consistent values when the two precessing models are compared. In addition, this analysis provides an estimate of the systematic error on precessing spin parameters such as the effective precession spin χ_p and the tilt angles ($\hat{S}_{1,2} \cdot \hat{L}_N$), which was not available in Ref. [2]. We have also carefully investigated uncertainties due to the finite numbers of samples used to recreate continuous posterior density functions, and we quantified their effects on quoted credible intervals. As in Ref. [2], the statistical error due to finite signal-to-noise ratio dominates the parameter-estimation error.

While we do recover a tighter limit on the spin magnitude of the most massive member of the binary that created GW150914 (< 0.65 at 90% probability), the recovery of the spin parameters (magnitude and tilt angles) is too broad to hint at whether the black hole binary was formed via stellar binary interactions or dynamical capture [18]. This analysis on the first direct detection by LIGO will be applied to future detections [59], with the aim of getting the most accurate and most precise parameter estimate possible. In particular, binaries that have larger mass asymmetry, that are observed for a longer time, and that are more edge-on than GW150914 will display stronger spin-precession effects.

ACKNOWLEDGMENTS

The authors gratefully acknowledge the support of the United States National Science Foundation (NSF) for the construction and operation of the LIGO Laboratory and Advanced LIGO as well as the Science and Technology Facilities Council (STFC) of the United Kingdom, the Max-Planck-Society (MPS), and the State of Niedersachsen/Germany for support of the construction of Advanced LIGO and construction and operation of the GEO 600 detector. Additional support for Advanced LIGO was provided by the Australian Research Council. The authors gratefully acknowledge the Italian Istituto Nazionale di Fisica Nucleare (INFN), the French Centre National de la Recherche Scientifique (CNRS) and the Foundation for Fundamental Research on Matter supported by the Netherlands Organisation for Scientific Research, for the construction and operation of the Virgo detector and the creation and support of the EGO consortium. The authors also gratefully acknowledge research support from these agencies as well as by the Council of Scientific and Industrial Research of India, Department of Science and Technology, India, Science & Engineering Research Board (SERB), India, Ministry of Human Resource Development, India, the Spanish Ministerio de

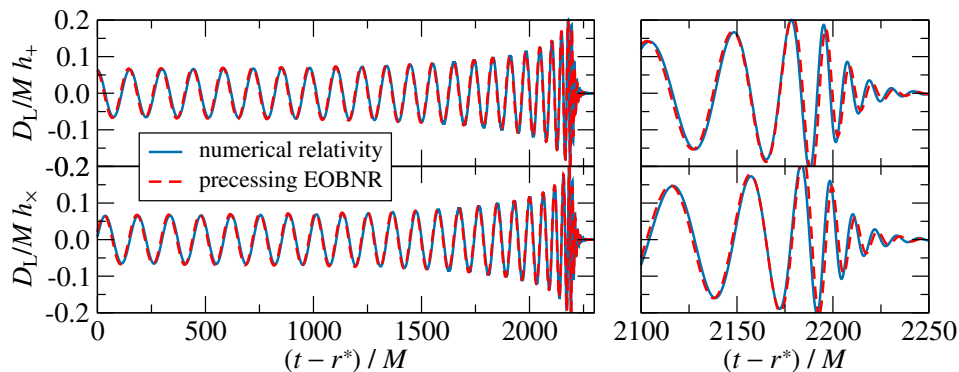


FIG. 7. A visual comparison of the precessing EOBNR model with NR GW polarizations computed by the SXS collaboration at (approximately) the GW150914 MaP parameters. The intrinsic parameters of the NR waveform are $q = 0.81$, $a_1 = 0.34$, $a_2 = 0.67$. The inclination is $\iota = 2.856$ rad. The alignment of the precessing EOBNR waveform is obtained from the sky- and polarization-averaged overlap with the NR waveform.

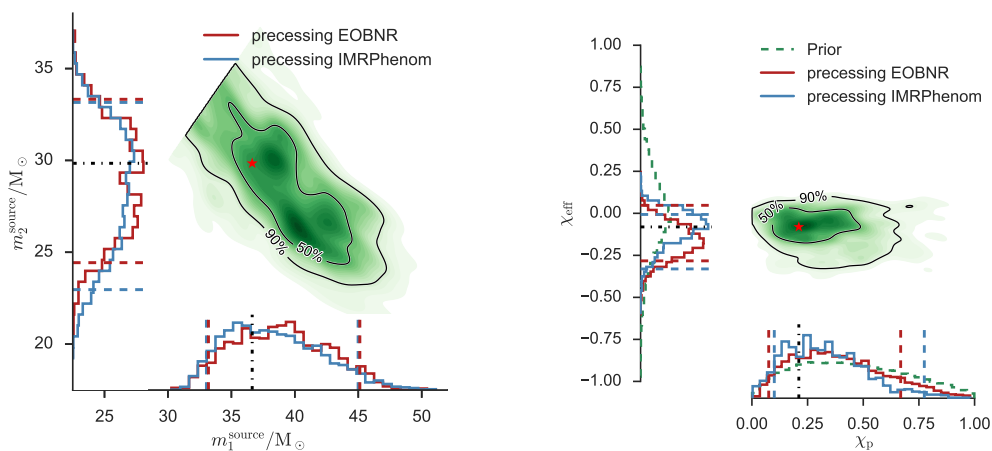


FIG. 8. Posterior probability densities for the source-frame component masses m_1^{source} and m_2^{source} , where $m_2^{\text{source}} \leq m_1^{\text{source}}$, (left) and effective aligned χ_{eff} and effective precessing spins χ_p (right) for an event-like NR mock signal close to MaP parameters. In the 1-dimensional marginalized distributions we show the precessing EOBNR (red) and precessing IMRPhenom (blue) probability densities with dashed vertical lines marking 90% credible intervals. The 2-dimensional plot shows the contours of the 50% and 90% credible regions of the precessing EOBNR over a color-coded posterior density function. The true parameter values are indicated by a red asterisk or black dot-dashed line.

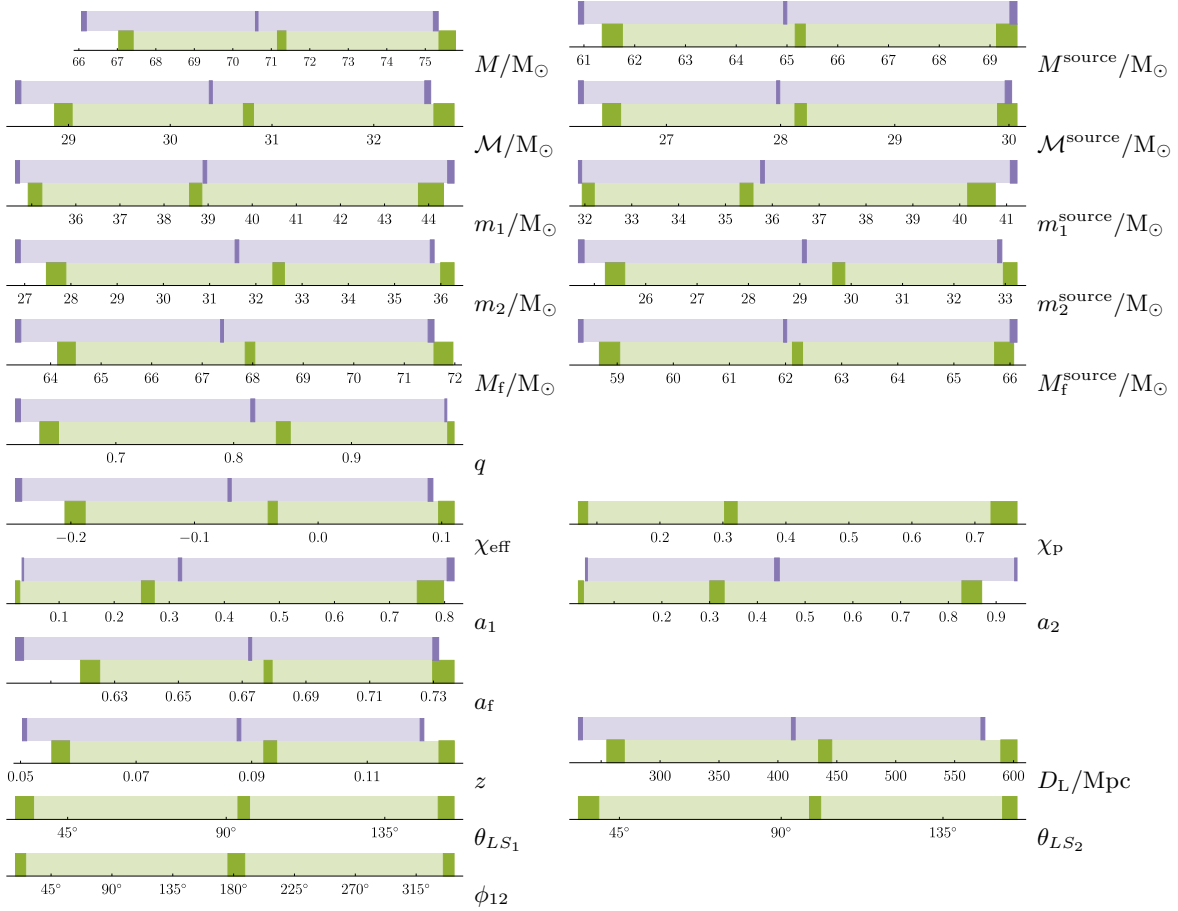
Economía y Competitividad, the Conselleria d’Economia i Competitivitat and Conselleria d’Educació, Cultura i Universitats of the Govern de les Illes Balears, the National Science Centre of Poland, the European Commission, the Royal Society, the Scottish Funding Council, the Scottish Universities Physics Alliance, the Hungarian Scientific Research Fund (OTKA), the Lyon Institute of Origins (LIO), the National Research Foundation of Korea, Industry Canada and the Province of Ontario through the Ministry of Economic Development and Innovation, the Natural Science and Engineering Research Council Canada, Canadian Institute for Advanced Research, the Brazilian Ministry of Science, Technology, and Innovation, Russian Foundation for Basic Research, the Leverhulme Trust, the Research Corporation, Ministry of Science and Technology (MOST), Taiwan and the Kavli Foundation. The authors gratefully acknowl-

edge the support of the NSF, STFC, MPS, INFN, CNRS and the State of Niedersachsen/Germany for provision of computational resources.

Appendix: Credible intervals for the combined posteriors

To compare directly with the results of Ref. [2], Table 9 presents the 90% credible intervals obtained with combined nonprecessing-EOBNR and precessing-IMRPhenom models, and with combined precessing-EOBNR precessing-IMRPhenom models. As in Table 1, the darker bands visualize uncertainties due the finite number of samples, as estimated with the Bayesian bootstrap.

FIG. 9. Comparison of parameter estimates obtained by combining the nonprecessing-EOBNR and precessing-IMRPhenom models (as in Ref. [2]; light purple bars at the top) and by combining the precessing-EOBNR and precessing-IMRPhenom models (light green bars at the bottom). We show 90% credible intervals for selected GW150914 source parameters. The darker intervals represent uncertainty estimates for the 5%, 50% and 95% quantiles (from left to right), as estimated by the Bayesian bootstrap.



- [1] B. P. Abbott *et al.* (LIGO Scientific Collaboration, Virgo Collaboration), Phys. Rev. Lett. **116**, 061102 (2016), <https://dcc.ligo.org/LIGO-P150914/public/main>, arXiv:1602.03847 [gr-qc].
- [2] B. P. Abbott *et al.* (LIGO Scientific Collaboration, Virgo Collaboration), (2016), <https://dcc.ligo.org/LIGO-P1500218/public/main>, arXiv:1602.03840 [gr-qc].
- [3] B. Bruegmann, J. A. Gonzalez, M. Hannam, S. Husa, U. Sperhake, and W. Tichy, Phys. Rev. **D77**, 024027 (2008), arXiv:gr-qc/0610128 [gr-qc].
- [4] R. O’Shaughnessy, L. London, J. Healy, and D. Shoemaker, Phys. Rev. **D87**, 044038 (2013), arXiv:1209.3712 [gr-qc].
- [5] M. A. Scheel, M. Giesler, D. A. Hemberger, G. Lovelace, K. Kuper, M. Boyle, B. Szilágyi, and L. E. Kidder, Class. Quant. Grav. **32**, 105009 (2015), arXiv:1412.1803 [gr-qc].
- [6] T. Chu, H. Fong, P. Kumar, H. P. Pfeiffer, M. Boyle, D. A. Hemberger, L. E. Kidder, M. A. Scheel, and B. Szilágyi, “On the accuracy and precision of numerical waveforms: Effect of waveform extraction methodology,” (2015), arXiv:1512.06800.
- [7] C. O. Lousto, J. Healy, and H. Nakano, “Spin flips in generic black hole binaries,” (2015), arXiv:1508.04768.
- [8] B. Szilágyi, J. Blackman, A. Buonanno, A. Taracchini, H. P. Pfeiffer, M. A. Scheel, T. Chu, L. E. Kidder, and Y. Pan, Phys. Rev. Lett. **115**, 031102 (2015), arXiv:1502.04953 [gr-qc].
- [9] P. Kumar, K. Barkett, S. Bhagwat, N. Afshari, D. A. Brown, G. Lovelace, M. A. Scheel, and B. Szilgyi, Phys. Rev. **D92**, 102001 (2015), arXiv:1507.00103 [gr-qc].
- [10] C. O. Lousto and J. Healy, Phys. Rev. Lett. **114**, 141101 (2015), arXiv:1410.3830 [gr-qc].
- [11] A. Buonanno and T. Damour, Phys. Rev. **D59**, 084006 (1999), arXiv:gr-qc/9811091 [gr-qc].
- [12] A. Buonanno and T. Damour, Phys. Rev. **D62**, 064015 (2000), arXiv:gr-qc/0001013 [gr-qc].
- [13] A. Taracchini *et al.*, Phys. Rev. **D89**, 061502 (2014), arXiv:1311.2544 [gr-qc].
- [14] M. Hannam, Gen. Rel. Grav. **46**, 1767 (2014), arXiv:1312.3641 [gr-qc].

- [15] Y. Pan, A. Buonanno, A. Taracchini, L. E. Kidder, A. H. Mroué, H. P. Pfeiffer, M. A. Scheel, and B. Szilgyi, *Phys. Rev.* **D89**, 084006 (2014), arXiv:1307.6232 [gr-qc].
- [16] S. Babak, A. Taracchini, and A. Buonanno, In preparation (2016).
- [17] J. Aasi *et al.* (LIGO Collaboration, Virgo Collaboration), *Phys. Rev.* **D88**, 062001 (2013), arXiv:1304.1775 [gr-qc].
- [18] B. P. Abbott *et al.* (LIGO Scientific Collaboration, Virgo Collaboration), *Astrophys. J.* **818**, L22 (2016), <https://dcc.ligo.org/LIGO-P1500262/public/main>, arXiv:1602.03846 [astro-ph.HE].
- [19] T. Damour, *Phys. Rev.* **D64**, 124013 (2001), arXiv:gr-qc/0103018 [gr-qc].
- [20] A. Buonanno, Y. Chen, and T. Damour, *Phys. Rev.* **D74**, 104005 (2006), arXiv:gr-qc/0508067 [gr-qc].
- [21] T. Damour, P. Jaranowski, and G. Schafer, *Phys. Rev.* **D78**, 024009 (2008), arXiv:0803.0915 [gr-qc].
- [22] E. Barausse and A. Buonanno, *Phys. Rev.* **D81**, 084024 (2010), arXiv:0912.3517 [gr-qc].
- [23] E. Barausse and A. Buonanno, *Phys. Rev.* **D84**, 104027 (2011), arXiv:1107.2904 [gr-qc].
- [24] T. Damour and A. Nagar, *Phys. Rev.* **D90**, 044018 (2014), arXiv:1406.6913 [gr-qc].
- [25] L. Blanchet, *Living Rev. Rel.* **17**, 2 (2014).
- [26] T. Damour and A. Nagar, *Phys. Rev.* **D76**, 064028 (2007), arXiv:0705.2519 [gr-qc].
- [27] T. Damour, B. R. Iyer, and A. Nagar, *Phys. Rev.* **D79**, 064004 (2009), arXiv:0811.2069 [gr-qc].
- [28] Y. Pan, A. Buonanno, R. Fujita, E. Racine, and H. Tagoshi, *Phys. Rev.* **D83**, 064003 (2011), [Erratum: *Phys. Rev.* D87, no.10, 109901(2013)], arXiv:1006.0431 [gr-qc].
- [29] C. V. Vishveshwara, *Nature* **227**, 936 (1970).
- [30] W. H. Press, *Astrophys. J.* **170**, L105 (1971).
- [31] S. Chandrasekhar and S. L. Detweiler, *Proc. Roy. Soc. Lond.* **A344**, 441 (1975).
- [32] A. H. Mroué *et al.*, *Phys. Rev. Lett.* **111**, 241104 (2013), arXiv:1304.6077 [gr-qc].
- [33] E. Barausse, A. Buonanno, S. A. Hughes, G. Khanna, S. O’Sullivan, and Y. Pan, *Phys. Rev.* **D85**, 024046 (2012), arXiv:1110.3081 [gr-qc].
- [34] A. Taracchini, A. Buonanno, G. Khanna, and S. A. Hughes, *Phys. Rev.* **D90**, 084025 (2014), arXiv:1404.1819 [gr-qc].
- [35] A. Buonanno, Y.-b. Chen, Y. Pan, and M. Vallisneri, *Phys. Rev. D* **70**, 104003 (2004), erratum-ibid. 74 (2006) 029902(E), gr-qc/0405090.
- [36] M. Boyle, R. Owen, and H. P. Pfeiffer, *Phys. Rev.* **D84**, 124011 (2011), arXiv:1110.2965 [gr-qc].
- [37] P. Schmidt, M. Hannam, S. Husa, and P. Ajith, *Phys. Rev.* **D84**, 024046 (2011), arXiv:1012.2879 [gr-qc].
- [38] R. O’Shaughnessy, B. Vaishnav, J. Healy, Z. Meeks, and D. Shoemaker, *Phys. Rev.* **D84**, 124002 (2011), arXiv:1109.5224 [gr-qc].
- [39] P. Schmidt, M. Hannam, and S. Husa, *Phys. Rev.* **D86**, 104063 (2012), arXiv:1207.3088 [gr-qc].
- [40] P. Schmidt, F. Ohme, and M. Hannam, *Phys. Rev.* **D91**, 024043 (2015), arXiv:1408.1810 [gr-qc].
- [41] M. Hannam, P. Schmidt, A. Bohé, L. Haegel, S. Husa, F. Ohme, G. Pratten, and M. Pürrer, *Phys. Rev. Lett.* **113**, 151101 (2014), arXiv:1308.3271 [gr-qc].
- [42] S. Khan, S. Husa, M. Hannam, F. Ohme, M. Pürrer, X. J. Forteza, and A. Bohé, “Frequency-domain gravitational waves from non-precessing black-hole binaries. II. A phenomenological model for the advanced detector era,” (2015), arXiv:1508.07253.
- [43] P. Kumar, T. Chu, H. Fong, H. P. Pfeiffer, M. Boyle, D. A. Hemberger, L. E. Kidder, M. A. Scheel, and B. Szilágyi, “Accuracy of binary black hole waveform models for aligned-spin binaries,” (2016), arXiv:1601.05396.
- [44] T. Bayes and R. Price, *Phil. Trans. Roy. Soc. Lond.* **53**, 370 (1763).
- [45] E. T. Jaynes, *Probability Theory: The Logic of Science*, edited by G. L. Bretthorst (Cambridge University Press, Cambridge, 2003).
- [46] J. Veitch *et al.*, *Phys. Rev.* **D91**, 042003 (2015), arXiv:1409.7215 [gr-qc].
- [47] C. Cutler and E. E. Flanagan, *Phys. Rev.* **D49**, 2658 (1994), arXiv:gr-qc/9402014 [gr-qc].
- [48] B. P. Abbott *et al.* (LIGO Scientific Collaboration), (2016), <https://dcc.ligo.org/LIGO-P1500248/public/main>, arXiv:1602.03845 [gr-qc].
- [49] J. Veitch and W. Del Pozzo, *Analytic marginalisation of phase parameter*, Tech. Rep. LIGO-T1300326 (LIGO Scientific Collaboration and Virgo Collaboration, 2013).
- [50] D. B. Rubin, *Ann. Statist.* **9**, 130 (1981).
- [51] N. K. Johnson-McDaniel *et al.*, *Determining the final spin of a binary black hole system including in-plane spins: Method and checks of accuracy*, Tech. Rep. LIGO-T1600168 (LIGO Project, 2016).
- [52] E. Racine, *Phys. Rev.* **D78**, 044021 (2008), arXiv:0803.1820 [gr-qc].
- [53] P. Ajith *et al.*, *Phys. Rev. Lett.* **106**, 241101 (2011), arXiv:0909.2867 [gr-qc].
- [54] L. Santamaría, F. Ohme, P. Ajith, B. Brügmann, N. Dorband, M. Hannam, S. Husa, P. Moesta, D. Pollney, C. Reisswig, E. L. Robinson, J. Seiler, and B. Krishnan, *Phys. Rev. D* **82**, 064016 (2010), arXiv:1005.3306 [gr-qc].
- [55] P. Schmidt and I. Harry, “Numerical Relativity Injection Infrastructure,” (2016), (in preparation).
- [56] P. Schmidt and C. Galley, “Reduced-order spline interpolants of Numerical Relativity waveforms,” (2016), (in preparation).
- [57] <http://www.black-holes.org/SpEC.html>.
- [58] <http://www.black-holes.org/waveforms>.
- [59] B. P. Abbott *et al.* (LIGO Scientific Collaboration, Virgo Collaboration), (2016), <https://dcc.ligo.org/LIGO-P1500217/public/main>, arXiv:1602.03842 [astro-ph.HE].

Authors

B. P. Abbott,¹ R. Abbott,¹ T. D. Abbott,² M. R. Abernathy,³ F. Acernese,^{4,5} K. Ackley,⁶ C. Adams,⁷ T. Adams,⁸ P. Addesso,⁹ R. X. Adhikari,¹ V. B. Adya,¹⁰ C. Affeldt,¹⁰ M. Agathos,¹¹ K. Agatsuma,¹¹ N. Aggarwal,¹² O. D. Aguiar,¹³ L. Aiello,^{14,15} A. Ain,¹⁶ P. Ajith,¹⁷ B. Allen,^{10,18,19} A. Allocca,^{20,21} P. A. Altin,²² S. B. Anderson,¹ W. G. Anderson,¹⁸ K. Arai,¹ M. C. Araya,¹ C. C. Arceneaux,²³ J. S. Areeda,²⁴ N. Arnaud,²⁵ K. G. Arun,²⁶ S. Ascenzi,^{27,15} G. Ashton,²⁸ M. Ast,²⁹ S. M. Aston,⁷ P. Astone,³⁰ P. Aufmuth,¹⁹ C. Aulbert,¹⁰ S. Babak,³¹ P. Bacon,³² M. K. M. Bader,¹¹ P. T. Baker,³³ F. Baldaccini,^{34,35} G. Ballardin,³⁶ S. W. Ballmer,³⁷ J. C. Barayoga,¹ S. E. Barclay,³⁸ B. C. Barish,¹ D. Barker,³⁹ F. Barone,^{4,5} B. Barr,³⁸ L. Barsotti,¹² M. Barsuglia,³² D. Barta,⁴⁰ J. Bartlett,³⁹ I. Bartos,⁴¹ R. Bassiri,⁴² A. Basti,^{20,21} J. C. Batch,³⁹ C. Baune,¹⁰ V. Bavigadda,³⁶ M. Bazzan,^{43,44} M. Bejger,⁴⁵ A. S. Bell,³⁸ B. K. Berger,¹ G. Bergmann,¹⁰ C. P. L. Berry,⁴⁶ D. Bersanetti,^{47,48} A. Bertolini,¹¹ J. Betzwieser,⁷ S. Bhagwat,³⁷ R. Bhandare,⁴⁹ I. A. Bilenko,⁵⁰ G. Billingsley,¹ J. Birch,⁷ R. Birney,⁵¹ O. Birnholtz,¹⁰ S. Biscans,¹² A. Bisht,^{10,19} M. Bitossi,³⁶ C. Biwer,³⁷ M. A. Bizouard,²⁵ J. K. Blackburn,¹ C. D. Blair,⁵² D. G. Blair,⁵² R. M. Blair,³⁹ S. Bloemen,⁵³ O. Bock,¹⁰ M. Boer,⁵⁴ G. Bogaert,⁵⁴ C. Bogan,¹⁰ A. Bohe,³¹ C. Bond,⁴⁶ F. Bondu,⁵⁵ R. Bonnand,⁸ B. A. Boom,¹¹ R. Bork,¹ V. Boschi,^{20,21} S. Bose,^{56,16} Y. Bouffanais,³² A. Bozzi,³⁶ C. Bradaschia,²¹ P. R. Brady,¹⁸ V. B. Braginsky,⁵⁰ M. Branchesi,^{57,58} J. E. Brau,⁵⁹ T. Briant,⁶⁰ A. Brillet,⁵⁴ M. Brinkmann,¹⁰ V. Brisson,²⁵ P. Brockill,¹⁸ J. E. Broida,⁶¹ A. F. Brooks,¹ D. A. Brown,³⁷ D. D. Brown,⁴⁶ N. M. Brown,¹² S. Brunett,¹ C. C. Buchanan,² A. Buikema,¹² T. Bulik,⁶² H. J. Bulten,^{63,11} A. Buonanno,^{31,64} D. Buskalic,⁸ C. Buy,³² R. L. Byer,⁴² M. Cabero,¹⁰ L. Cadonati,⁶⁵ G. Cagnoli,^{66,67} C. Cahillane,¹ J. Calderón Bustillo,⁶⁵ T. Callister,¹ E. Calloni,^{68,5} J. B. Camp,⁶⁹ K. C. Cannon,⁷⁰ J. Cao,⁷¹ C. D. Capano,¹⁰ E. Capocasa,³² F. Carbognani,³⁶ S. Caride,⁷² J. Casanueva Diaz,²⁵ C. Casentini,^{27,15} S. Caudill,¹⁸ M. Cavaglia,²³ F. Cavalier,²⁵ R. Cavalieri,³⁶ G. Cella,²¹ C. B. Cepeda,¹ L. Cerboni Baiardi,^{57,58} G. Cerretani,^{20,21} E. Cesarini,^{27,15} M. Chan,³⁸ S. Chao,⁷³ P. Charlton,⁷⁴ E. Chassande-Mottin,³² B. D. Cheeseboro,⁷⁵ H. Y. Chen,⁷⁶ Y. Chen,⁷⁷ C. Cheng,⁷³ A. Chincarini,⁴⁸ A. Chiummo,³⁶ H. S. Cho,⁷⁸ M. Cho,⁶⁴ J. H. Chow,²² N. Christensen,⁶¹ Q. Chu,⁵² S. Chua,⁶⁰ S. Chung,⁵² G. Ciani,⁶ F. Clara,³⁹ J. A. Clark,⁶⁵ F. Cleva,⁵⁴ E. Coccia,^{27,14} P.-F. Cohadon,⁶⁰ A. Colla,^{79,30} C. G. Collette,⁸⁰ L. Cominsky,⁸¹ M. Constancio Jr.,¹³ A. Conte,^{79,30} L. Conti,⁴⁴ D. Cook,³⁹ T. R. Corbitt,² N. Cornish,³³ A. Corsi,⁷² S. Cortese,³⁶ C. A. Costa,¹³ M. W. Coughlin,⁶¹ S. B. Coughlin,⁸² J.-P. Coulon,⁵⁴ S. T. Countryman,⁴¹ P. Couvares,¹ E. E. Cowan,⁶⁵ D. M. Coward,⁵² M. J. Cowart,⁷ D. C. Coyne,¹ R. Coyne,⁷² K. Craig,³⁸ J. D. E. Creighton,¹⁸ J. Cripe,² S. G. Crowder,⁸³ A. Cumming,³⁸ L. Cunningham,³⁸ E. Cuoco,³⁶ T. Dal Canton,¹⁰ S. L. Danilishin,³⁸ S. D'Antonio,¹⁵ K. Danzmann,^{19,10} N. S. Darman,⁸⁴ A. Dasgupta,⁸⁵ C. F. Da Silva Costa,⁶ V. Dattilo,³⁶ I. Dave,⁴⁹ M. Davier,²⁵ G. S. Davies,³⁸ E. J. Daw,⁸⁶ R. Day,³⁶ S. De,³⁷ D. DeBra,⁴² G. Debreczeni,⁴⁰ J. Degallaix,⁶⁶ M. De Laurentis,^{68,5} S. Deléglise,⁶⁰ W. Del Pozzo,⁴⁶ T. Denker,¹⁰ T. Dent,¹⁰ V. Dergachev,¹ R. De Rosa,^{68,5} R. T. DeRosa,⁷ R. DeSalvo,⁹ R. C. Devine,⁷⁵ S. Dhurandhar,¹⁶ M. C. Díaz,⁸⁷ L. Di Fiore,⁵ M. Di Giovanni,^{88,89} T. Di Girolamo,^{68,5} A. Di Lieto,^{20,21} S. Di Pace,^{79,30} I. Di Palma,^{31,79,30} A. Di Virgilio,²¹ V. Dolique,⁶⁶ F. Donovan,¹² K. L. Dooley,²³ S. Doravari,¹⁰ R. Douglas,³⁸ T. P. Downes,¹⁸ M. Drago,¹⁰ R. W. P. Drever,¹ J. C. Driggers,³⁹ M. Ducrot,⁸ S. E. Dwyer,³⁹ T. B. Edo,⁸⁶ M. C. Edwards,⁶¹ A. Effler,⁷ H.-B. Eggenstein,¹⁰ P. Ehrens,¹ J. Eichholz,^{6,1} S. S. Eikenberry,⁶ W. Engels,⁷⁷ R. C. Essick,¹² Z. Etienne,⁷⁵ T. Etzel,¹ M. Evans,¹² T. M. Evans,⁷ R. Everett,⁹⁰ M. Factourovich,⁴¹ V. Fafone,^{27,15} H. Fair,³⁷ S. Fairhurst,⁹¹ X. Fan,⁷¹ Q. Fang,⁵² S. Farinon,⁴⁸ B. Farr,⁷⁶ W. M. Farr,⁴⁶ E. Fauchon-Jones,⁹¹ M. Favata,⁹² M. Fays,⁹¹ H. Fehrmann,¹⁰ M. M. Fejer,⁴² E. Fenyvesi,⁹³ I. Ferrante,^{20,21} E. C. Ferreira,¹³ F. Ferrini,³⁶ F. Fidecaro,^{20,21} I. Fiori,³⁶ D. Fiorucci,³² R. P. Fisher,³⁷ R. Flaminio,^{66,94} M. Fletcher,³⁸ J.-D. Fournier,⁵⁴ S. Frasca,^{79,30} F. Frasconi,²¹ Z. Frei,⁹³ A. Freise,⁴⁶ R. Frey,⁵⁹ V. Frey,²⁵ P. Fritschel,¹² V. V. Frolov,⁷ P. Fulda,⁶ M. Fyffe,⁷ H. A. G. Gabbard,²³ S. Gaebel,⁴⁶ J. R. Gair,⁹⁵ L. Gammaitoni,³⁴ S. G. Gaonkar,¹⁶ F. Garufi,^{68,5} G. Gaur,^{96,85} N. Gehrels,⁶⁹ G. Gemme,⁴⁸ P. Geng,⁸⁷ E. Genin,³⁶ A. Gennai,²¹ J. George,⁴⁹ L. Gergely,⁹⁷ V. Germain,⁸ Abhirup Ghosh,¹⁷ Archisman Ghosh,¹⁷ S. Ghosh,^{53,11} J. A. Giaime,^{2,7} K. D. Giardino,⁷ A. Giazotto,²¹ K. Gill,⁹⁸ A. Glaefke,³⁸ E. Goetz,³⁹ R. Goetz,⁶ L. Gondan,⁹³ G. González,² J. M. Gonzalez Castro,^{20,21} A. Gopakumar,⁹⁹ N. A. Gordon,³⁸ M. L. Gorodetsky,⁵⁰ S. E. Gossan,¹ M. Gosselin,³⁶ R. Gouaty,⁸ A. Grado,^{100,5} C. Graef,³⁸ P. B. Graff,⁶⁴ M. Granata,⁶⁶ A. Grant,³⁸ S. Gras,¹² C. Gray,³⁹ G. Greco,^{57,58} A. C. Green,⁴⁶ P. Groot,⁵³ H. Grote,¹⁰ S. Grunewald,³¹ G. M. Guidi,^{57,58} X. Guo,⁷¹ A. Gupta,¹⁶ M. K. Gupta,⁸⁵ K. E. Gushwa,¹ E. K. Gustafson,¹ R. Gustafson,¹⁰¹ R. Haas,³¹ J. J. Hacker,²⁴ B. R. Hall,⁵⁶ E. D. Hall,¹ G. Hammond,³⁸ M. Haney,⁹⁹ M. M. Hanke,¹⁰ J. Hanks,³⁹ C. Hanna,⁹⁰ M. D. Hannam,⁹¹ J. Hanson,⁷ T. Hardwick,² J. Harms,^{57,58} G. M. Harry,³ I. W. Harry,³¹ M. J. Hart,³⁸ M. T. Hartman,⁶ C.-J. Haster,⁴⁶ K. Haughian,³⁸ J. Healy,¹⁰² A. Heidmann,⁶⁰ M. C. Heintze,⁷ H. Heitmann,⁵⁴ P. Hello,²⁵ G. Hemming,³⁶ M. Hendry,³⁸ I. S. Heng,³⁸ J. Hennig,³⁸ J. Henry,¹⁰² A. W. Heptonstall,¹ M. Heurs,^{10,19} S. Hild,³⁸ I. Hinder,³¹ D. Hoak,³⁶ D. Hofman,⁶⁶

K. Holt,⁷ D. E. Holz,⁷⁶ P. Hopkins,⁹¹ J. Hough,³⁸ E. A. Houston,³⁸ E. J. Howell,⁵² Y. M. Hu,¹⁰ S. Huang,⁷³
 E. A. Huerta,¹⁰³ D. Huet,²⁵ B. Hughey,⁹⁸ S. Husa,¹⁰⁴ S. H. Huttner,³⁸ T. Huynh-Dinh,⁷ N. Indik,¹⁰ D. R. Ingram,³⁹
 R. Inta,⁷² H. N. Isa,³⁸ J.-M. Isac,⁶⁰ M. Isi,¹ T. Isogai,¹² B. R. Iyer,¹⁷ K. Izumi,³⁹ T. Jacqmin,⁶⁰ H. Jang,⁷⁸ K. Jani,⁶⁵
 P. Jaranowski,¹⁰⁵ S. Jawahar,¹⁰⁶ L. Jian,⁵² F. Jiménez-Forteza,¹⁰⁴ W. W. Johnson,² N. K. Johnson-McDaniel,¹⁷
 D. I. Jones,²⁸ R. Jones,³⁸ R. J. G. Jonker,¹¹ L. Ju,⁵² Haris K,¹⁰⁷ C. V. Kalaghatgi,⁹¹ V. Kalogera,⁸²
 S. Kandhasamy,²³ G. Kang,⁷⁸ J. B. Kanner,¹ S. J. Kapadia,¹⁰ S. Karki,⁵⁹ K. S. Karvinen,¹⁰ M. Kasprzack,^{36,2}
 E. Katsavounidis,¹² W. Katzman,⁷ S. Kaufer,¹⁹ T. Kaur,⁵² K. Kawabe,³⁹ F. Kéfélian,⁵⁴ M. S. Kehl,¹⁰⁸ D. Keitel,¹⁰⁴
 D. B. Kelley,³⁷ W. Kells,¹ R. Kennedy,⁸⁶ J. S. Key,⁸⁷ F. Y. Khalili,⁵⁰ I. Khan,¹⁴ S. Khan,⁹¹ Z. Khan,⁸⁵
 E. A. Khazanov,¹⁰⁹ N. Kijbunchoo,³⁹ Chi-Woong Kim,⁷⁸ Chunglee Kim,⁷⁸ J. Kim,¹¹⁰ K. Kim,¹¹¹ N. Kim,⁴²
 W. Kim,¹¹² Y.-M. Kim,¹¹⁰ S. J. Kimbrell,⁶⁵ E. J. King,¹¹² P. J. King,³⁹ J. S. Kissel,³⁹ B. Klein,⁸² L. Kleybolte,²⁹
 S. Klimenko,⁶ S. M. Koehlenbeck,¹⁰ S. Koley,¹¹ V. Kondrashov,¹ A. Kontos,¹² M. Korobko,²⁹ W. Z. Korth,¹
 I. Kowalska,⁶² D. B. Kozak,¹ V. Kringel,¹⁰ B. Krishnan,¹⁰ A. Królak,^{113,114} C. Krueger,¹⁹ G. Kuehn,¹⁰
 P. Kumar,¹⁰⁸ R. Kumar,⁸⁵ L. Kuo,⁷³ A. Kutynia,¹¹³ B. D. Lackey,³⁷ M. Landry,³⁹ J. Lange,¹⁰² B. Lantz,⁴²
 P. D. Lasky,¹¹⁵ M. Laxen,⁷ A. Lazzarini,¹ C. Lazzaro,⁴⁴ P. Leaci,^{79,30} S. Leavey,³⁸ E. O. Lebigot,^{32,71} C. H. Lee,¹¹⁰
 H. K. Lee,¹¹¹ H. M. Lee,¹¹⁶ K. Lee,³⁸ A. Lenon,³⁷ M. Leonardi,^{88,89} J. R. Leong,¹⁰ N. Leroy,²⁵ N. Letendre,⁸
 Y. Levin,¹¹⁵ J. B. Lewis,¹ T. G. F. Li,¹¹⁷ A. Libson,¹² T. B. Littenberg,¹¹⁸ N. A. Lockerbie,¹⁰⁶ A. L. Lombardi,¹¹⁹
 L. T. London,⁹¹ J. E. Lord,³⁷ M. Lorenzini,^{14,15} V. Lorette,¹²⁰ M. Lormand,⁷ G. Losurdo,⁵⁸ J. D. Lough,^{10,19}
 C. O. Lousto,¹⁰² G. Lovelace,²⁴ H. Lück,^{19,10} A. P. Lundgren,¹⁰ R. Lynch,¹² Y. Ma,⁵² B. Machenschalk,¹⁰
 M. MacInnis,¹² D. M. Macleod,² F. Magaña-Sandoval,³⁷ L. Magaña Zertuche,³⁷ R. M. Magee,⁵⁶ E. Majorana,³⁰
 I. Maksimovic,¹²⁰ V. Malvezzi,^{27,15} N. Man,⁵⁴ V. Mandic,⁸³ V. Mangano,³⁸ G. L. Mansell,²² M. Manske,¹⁸
 M. Mantovani,³⁶ F. Marchesoni,^{121,35} F. Marion,⁸ S. Márka,⁴¹ Z. Márka,⁴¹ A. S. Markosyan,⁴² E. Maros,¹
 F. Martelli,^{57,58} L. Martellini,⁵⁴ I. W. Martin,³⁸ D. V. Martynov,¹² J. N. Marx,¹ K. Mason,¹² A. Masserot,⁸
 T. J. Massinger,³⁷ M. Masso-Reid,³⁸ S. Mastrogiovanni,^{79,30} F. Matichard,¹² L. Matone,⁴¹ N. Mavalvala,¹²
 N. Mazumder,⁵⁶ R. McCarthy,³⁹ D. E. McClelland,²² S. McCormick,⁷ S. C. McGuire,¹²² G. McIntyre,¹ J. McIver,¹
 D. J. McManus,²² T. McRae,²² S. T. McWilliams,⁷⁵ D. Meacher,⁹⁰ G. D. Meadors,^{31,10} J. Meidam,¹¹ A. Melatos,⁸⁴
 G. Mendell,³⁹ R. A. Mercer,¹⁸ E. L. Merilh,³⁹ M. Merzougui,⁵⁴ S. Meshkov,¹ C. Messenger,³⁸ C. Messick,⁹⁰
 R. Metzdrorff,⁶⁰ P. M. Meyers,⁸³ F. Mezzani,^{30,79} H. Miao,⁴⁶ C. Michel,⁶⁶ H. Middleton,⁴⁶ E. E. Mikhailov,¹²³
 L. Milano,^{68,5} A. L. Miller,^{6,79,30} A. Miller,⁸² B. B. Miller,⁸² J. Miller,¹² M. Millhouse,³³ Y. Minenkov,¹⁵
 J. Ming,³¹ S. Mirshekari,¹²⁴ C. Mishra,¹⁷ S. Mitra,¹⁶ V. P. Mitrofanov,⁵⁰ G. Mitselmakher,⁶ R. Mittleman,¹²
 A. Moggi,²¹ M. Mohan,³⁶ S. R. P. Mohapatra,¹² M. Montani,^{57,58} B. C. Moore,⁹² C. J. Moore,¹²⁵ D. Moraru,³⁹
 G. Moreno,³⁹ S. R. Morriss,⁸⁷ K. Mossavi,¹⁰ B. Mours,⁸ C. M. Mow-Lowry,⁴⁶ G. Mueller,⁶ A. W. Muir,⁹¹
 Arunava Mukherjee,¹⁷ D. Mukherjee,¹⁸ S. Mukherjee,⁸⁷ N. Mukund,¹⁶ A. Mullavey,⁷ J. Munch,¹¹² D. J. Murphy,⁴¹
 P. G. Murray,³⁸ A. Mytidis,⁶ I. Nardecchia,^{27,15} L. Naticchioni,^{79,30} R. K. Nayak,¹²⁶ K. Nedkova,¹¹⁹
 G. Nelemans,^{53,11} T. J. N. Nelson,⁷ M. Neri,^{47,48} A. Neunzert,¹⁰¹ G. Newton,³⁸ T. T. Nguyen,²² A. B. Nielsen,¹⁰
 S. Nissanke,^{53,11} A. Nitz,¹⁰ F. Nocera,³⁶ D. Nolting,⁷ M. E. N. Normandin,⁸⁷ L. K. Nuttall,³⁷ J. Oberling,³⁹
 E. Ochsner,¹⁸ J. O'Dell,¹²⁷ E. Oelker,¹² G. H. Ogín,¹²⁸ J. J. Oh,¹²⁹ S. H. Oh,¹²⁹ F. Ohme,⁹¹ M. Oliver,¹⁰⁴
 P. Oppermann,¹⁰ Richard J. Oram,⁷ B. O'Reilly,⁷ R. O'Shaughnessy,¹⁰² D. J. Ottaway,¹¹² H. Overmier,⁷
 B. J. Owen,⁷² A. Pai,¹⁰⁷ S. A. Pai,⁴⁹ J. R. Palamos,⁵⁹ O. Palashov,¹⁰⁹ C. Palomba,³⁰ A. Pal-Singh,²⁹ H. Pan,⁷³
 C. Pankow,⁸² F. Pannarale,⁹¹ B. C. Pant,⁴⁹ F. Paoletti,^{36,21} A. Paoli,³⁶ M. A. Papa,^{31,18,10} H. R. Paris,⁴²
 W. Parker,⁷ D. Pascucci,³⁸ A. Pasqualetti,³⁶ R. Passaquieti,^{20,21} D. Passuello,²¹ B. Patricelli,^{20,21} Z. Patrick,⁴²
 B. L. Pearlstone,³⁸ M. Pedraza,¹ R. Pedurand,^{66,130} L. Pekowsky,³⁷ A. Pele,⁷ S. Penn,¹³¹ A. Perreca,¹ L. M. Perri,⁸²
 H. P. Pfeiffer,^{108,31} M. Phelps,³⁸ O. J. Piccinni,^{79,30} M. Pichot,⁵⁴ F. Piergiovanni,^{57,58} V. Pierro,⁹ G. Pillant,³⁶
 L. Pinard,⁶⁶ I. M. Pinto,⁹ M. Pitkin,³⁸ M. Poe,¹⁸ R. Poggiani,^{20,21} P. Popolizio,³⁶ A. Post,¹⁰ J. Powell,³⁸
 J. Prasad,¹⁶ V. Predoi,⁹¹ T. Prestegard,⁸³ L. R. Price,¹ M. Prijatelj,^{10,36} M. Principe,⁹ S. Privitera,³¹ R. Prix,¹⁰
 G. A. Prodi,^{88,89} L. Prokhorov,⁵⁰ O. Puncken,¹⁰ M. Punturo,³⁵ P. Puppo,³⁰ M. Pürerer,³¹ H. Qi,¹⁸ J. Qin,⁵²
 S. Qiu,¹¹⁵ V. Quetschke,⁸⁷ E. A. Quintero,¹ R. Quitzow-James,⁵⁹ F. J. Raab,³⁹ D. S. Rabeling,²² H. Radkins,³⁹
 P. Raffai,⁹³ S. Raja,⁴⁹ C. Rajan,⁴⁹ M. Rakhmanov,⁸⁷ P. Rapagnani,^{79,30} V. Raymond,³¹ M. Razzano,^{20,21} V. Re,²⁷
 J. Read,²⁴ C. M. Reed,³⁹ T. Regimbau,⁵⁴ L. Rei,⁴⁸ S. Reid,⁵¹ D. H. Reitze,^{1,6} H. Rew,¹²³ S. D. Reyes,³⁷
 F. Ricci,^{79,30} K. Riles,¹⁰¹ M. Rizzo,¹⁰² N. A. Robertson,^{1,38} R. Robie,³⁸ F. Robinet,²⁵ A. Rocchi,¹⁵ L. Rolland,⁸
 J. G. Rollins,¹ V. J. Roma,⁵⁹ J. D. Romano,⁸⁷ R. Romano,^{4,5} G. Romanov,¹²³ J. H. Romie,⁷ D. Rosińska,^{132,45}
 S. Rowan,³⁸ A. Rüdiger,¹⁰ P. Ruggi,³⁶ K. Ryan,³⁹ S. Sachdev,¹ T. Sadecki,³⁹ L. Sadeghian,¹⁸ M. Sakellariadou,¹³³
 L. Salconi,³⁶ M. Saleem,¹⁰⁷ F. Salemi,¹⁰ A. Samajdar,¹²⁶ L. Sammut,¹¹⁵ E. J. Sanchez,¹ V. Sandberg,³⁹
 B. Sandeen,⁸² J. R. Sanders,³⁷ B. Sassolas,⁶⁶ B. S. Sathyaprakash,⁹¹ P. R. Saulson,³⁷ O. E. S. Sauter,¹⁰¹

R. L. Savage,³⁹ A. Sawadsky,¹⁹ P. Schale,⁵⁹ R. Schilling[†],¹⁰ J. Schmidt,¹⁰ P. Schmidt,^{1,77} R. Schnabel,²⁹
R. M. S. Schofield,⁵⁹ A. Schönbeck,²⁹ E. Schreiber,¹⁰ D. Schuette,^{10,19} B. F. Schutz,^{91,31} J. Scott,³⁸ S. M. Scott,²²
D. Sellers,⁷ A. S. Sengupta,⁹⁶ D. Sentenac,³⁶ V. Sequino,^{27,15} A. Sergeev,¹⁰⁹ Y. Setyawati,^{53,11} D. A. Shaddock,²²
T. Shaffer,³⁹ M. S. Shahriar,⁸² M. Shaltev,¹⁰ B. Shapiro,⁴² P. Shawhan,⁶⁴ A. Sheperd,¹⁸ D. H. Shoemaker,¹²
D. M. Shoemaker,⁶⁵ K. Siellez,⁶⁵ X. Siemens,¹⁸ M. Sieniawska,⁴⁵ D. Sigg,³⁹ A. D. Silva,¹³ A. Singer,¹
L. P. Singer,⁶⁹ A. Singh,^{31,10,19} R. Singh,² A. Singhal,¹⁴ A. M. Sintes,¹⁰⁴ B. J. J. Slagmolen,²² J. R. Smith,²⁴
N. D. Smith,¹ R. J. E. Smith,¹ E. J. Son,¹²⁹ B. Sorazu,³⁸ F. Sorrentino,⁴⁸ T. Souradeep,¹⁶ A. K. Srivastava,⁸⁵
A. Staley,⁴¹ M. Steinke,¹⁰ J. Steinlechner,³⁸ S. Steinlechner,³⁸ D. Steinmeyer,^{10,19} B. C. Stephens,¹⁸
S. P. Stevenson,⁴⁶ R. Stone,⁸⁷ K. A. Strain,³⁸ N. Straniero,⁶⁶ G. Stratta,^{57,58} N. A. Strauss,⁶¹ S. Strigin,⁵⁰
R. Sturani,¹²⁴ A. L. Stuver,⁷ T. Z. Summerscales,¹³⁴ L. Sun,⁸⁴ S. Sunil,⁸⁵ P. J. Sutton,⁹¹ B. L. Swinkels,³⁶
M. J. Szczepańczyk,⁹⁸ M. Tacca,³² D. Talukder,⁵⁹ D. B. Tanner,⁶ M. Tápai,⁹⁷ S. P. Tarabrin,¹⁰ A. Taracchini,³¹
R. Taylor,¹ T. Theeg,¹⁰ M. P. Thirugnanasambandam,¹ E. G. Thomas,⁴⁶ M. Thomas,⁷ P. Thomas,³⁹
K. A. Thorne,⁷ K. S. Thorne,⁷⁷ E. Thrane,¹¹⁵ S. Tiwari,^{14,89} V. Tiwari,⁹¹ K. V. Tokmakov,¹⁰⁶ K. Toland,³⁸
C. Tomlinson,⁸⁶ M. Tonelli,^{20,21} Z. Tornasi,³⁸ C. V. Torres[‡],⁸⁷ C. I. Torrie,¹ D. Töyrä,⁴⁶ F. Travasso,^{34,35}
G. Traylor,⁷ D. Trifirò,²³ M. C. Tringali,^{88,89} L. Trozzo,^{135,21} M. Tse,¹² M. Turconi,⁵⁴ D. Tuyenbayev,⁸⁷
D. Ugolini,¹³⁶ C. S. Unnikrishnan,⁹⁹ A. L. Urban,¹⁸ S. A. Usman,³⁷ H. Vahlbruch,¹⁹ G. Vajente,¹ G. Valdes,⁸⁷
M. Vallisneri,⁷⁷ N. van Bakel,¹¹ M. van Beuzekom,¹¹ J. F. J. van den Brand,^{63,11} C. Van Den Broeck,¹¹
D. C. Vander-Hyde,³⁷ L. van der Schaaf,¹¹ M. V. van der Sluys,⁵³ J. V. van Heijningen,¹¹ A. Vano-Vinuales,⁹¹
A. A. van Veggel,³⁸ M. Vardaro,^{43,44} S. Vass,¹ M. Vasúth,⁴⁰ R. Vaulin,¹² A. Vecchio,⁴⁶ G. Vedovato,⁴⁴ J. Veitch,⁴⁶
P. J. Veitch,¹¹² K. Venkateswara,¹³⁷ D. Verkindt,⁸ F. Vetrano,^{57,58} A. Viceré,^{57,58} S. Vinciguerra,⁴⁶
D. J. Vine,⁵¹ J.-Y. Vinet,⁵⁴ S. Vitale,¹² T. Vo,³⁷ H. Vocca,^{34,35} C. Vorvick,³⁹ D. V. Voss,⁶ W. D. Voudsen,⁴⁶
S. P. Vyatchanin,⁵⁰ A. R. Wade,²² L. E. Wade,¹³⁸ M. Wade,¹³⁸ M. Walker,² L. Wallace,¹ S. Walsh,^{31,10}
G. Wang,^{14,58} H. Wang,⁴⁶ M. Wang,⁴⁶ X. Wang,⁷¹ Y. Wang,⁵² R. L. Ward,²² J. Warner,³⁹ M. Was,⁸ B. Weaver,³⁹
L.-W. Wei,⁵⁴ M. Weinert,¹⁰ A. J. Weinstein,¹ R. Weiss,¹² L. Wen,⁵² P. Weßels,¹⁰ T. Westphal,¹⁰ K. Wette,¹⁰
J. T. Whelan,¹⁰² B. F. Whiting,⁶ R. D. Williams,¹ A. R. Williamson,⁹¹ J. L. Willis,¹³⁹ B. Willke,^{19,10}
M. H. Wimmer,^{10,19} W. Winkler,¹⁰ C. C. Wipf,¹ H. Wittel,^{10,19} G. Woan,³⁸ J. Woehler,¹⁰ J. Worden,³⁹
J. L. Wright,³⁸ D. S. Wu,¹⁰ G. Wu,⁷ J. Yablon,⁸² W. Yam,¹² H. Yamamoto,¹ C. C. Yancey,⁶⁴ H. Yu,¹² M. Yvert,⁸
A. Zadrożny,¹¹³ L. Zangrando,⁴⁴ M. Zanolin,⁹⁸ J.-P. Zendri,⁴⁴ M. Zevin,⁸² L. Zhang,¹ M. Zhang,¹²³
Y. Zhang,¹⁰² C. Zhao,⁵² M. Zhou,⁸² Z. Zhou,⁸² X. J. Zhu,⁵² M. E. Zucker,^{1,12} S. E. Zuraw,¹¹⁹ and J. Zweizig¹

(LIGO Scientific Collaboration and Virgo Collaboration)

[†]Deceased, May 2015. [‡]Deceased, March 2015.

¹LIGO, California Institute of Technology, Pasadena, CA 91125, USA

²Louisiana State University, Baton Rouge, LA 70803, USA

³American University, Washington, D.C. 20016, USA

⁴Università di Salerno, Fisciano, I-84084 Salerno, Italy

⁵INFN, Sezione di Napoli, Complesso Universitario di Monte S. Angelo, I-80126 Napoli, Italy

⁶University of Florida, Gainesville, FL 32611, USA

⁷LIGO Livingston Observatory, Livingston, LA 70754, USA

⁸Laboratoire d'Annecy-le-Vieux de Physique des Particules (LAPP),
Université Savoie Mont Blanc, CNRS/IN2P3, F-74941 Annecy-le-Vieux, France

⁹University of Sannio at Benevento, I-82100 Benevento,
Italy and INFN, Sezione di Napoli, I-80100 Napoli, Italy

¹⁰Albert-Einstein-Institut, Max-Planck-Institut für Gravitationsphysik, D-30167 Hannover, Germany

¹¹Nikhef, Science Park, 1098 XG Amsterdam, The Netherlands

¹²LIGO, Massachusetts Institute of Technology, Cambridge, MA 02139, USA

¹³Instituto Nacional de Pesquisas Espaciais, 12227-010 São José dos Campos, São Paulo, Brazil

¹⁴INFN, Gran Sasso Science Institute, I-67100 L'Aquila, Italy

¹⁵INFN, Sezione di Roma Tor Vergata, I-00133 Roma, Italy

¹⁶Inter-University Centre for Astronomy and Astrophysics, Pune 411007, India

¹⁷International Centre for Theoretical Sciences, Tata Institute of Fundamental Research, Bangalore 560012, India

¹⁸University of Wisconsin-Milwaukee, Milwaukee, WI 53201, USA

¹⁹Leibniz Universität Hannover, D-30167 Hannover, Germany

²⁰Università di Pisa, I-56127 Pisa, Italy

²¹INFN, Sezione di Pisa, I-56127 Pisa, Italy

²²Australian National University, Canberra, Australian Capital Territory 0200, Australia

²³The University of Mississippi, University, MS 38677, USA

- ²⁴ *California State University Fullerton, Fullerton, CA 92831, USA*
- ²⁵ *LAL, Univ. Paris-Sud, CNRS/IN2P3, Université Paris-Saclay, Orsay, France*
- ²⁶ *Chennai Mathematical Institute, Chennai 603103, India*
- ²⁷ *Università di Roma Tor Vergata, I-00133 Roma, Italy*
- ²⁸ *University of Southampton, Southampton SO17 1BJ, United Kingdom*
- ²⁹ *Universität Hamburg, D-22761 Hamburg, Germany*
- ³⁰ *INFN, Sezione di Roma, I-00185 Roma, Italy*
- ³¹ *Albert-Einstein-Institut, Max-Planck-Institut für Gravitationsphysik, D-14476 Potsdam-Golm, Germany*
- ³² *APC, AstroParticule et Cosmologie, Université Paris Diderot, CNRS/IN2P3, CEA/Irfu, Observatoire de Paris, Sorbonne Paris Cité, F-75205 Paris Cedex 13, France*
- ³³ *Montana State University, Bozeman, MT 59717, USA*
- ³⁴ *Università di Perugia, I-06123 Perugia, Italy*
- ³⁵ *INFN, Sezione di Perugia, I-06123 Perugia, Italy*
- ³⁶ *European Gravitational Observatory (EGO), I-56021 Cascina, Pisa, Italy*
- ³⁷ *Syracuse University, Syracuse, NY 13244, USA*
- ³⁸ *SUPA, University of Glasgow, Glasgow G12 8QQ, United Kingdom*
- ³⁹ *LIGO Hanford Observatory, Richland, WA 99352, USA*
- ⁴⁰ *Wigner RCP, RMKI, H-1121 Budapest, Konkoly Thege Miklós út 29-33, Hungary*
- ⁴¹ *Columbia University, New York, NY 10027, USA*
- ⁴² *Stanford University, Stanford, CA 94305, USA*
- ⁴³ *Università di Padova, Dipartimento di Fisica e Astronomia, I-35131 Padova, Italy*
- ⁴⁴ *INFN, Sezione di Padova, I-35131 Padova, Italy*
- ⁴⁵ *CAMK-PAN, 00-716 Warsaw, Poland*
- ⁴⁶ *University of Birmingham, Birmingham B15 2TT, United Kingdom*
- ⁴⁷ *Università degli Studi di Genova, I-16146 Genova, Italy*
- ⁴⁸ *INFN, Sezione di Genova, I-16146 Genova, Italy*
- ⁴⁹ *RRCAT, Indore MP 452013, India*
- ⁵⁰ *Faculty of Physics, Lomonosov Moscow State University, Moscow 119991, Russia*
- ⁵¹ *SUPA, University of the West of Scotland, Paisley PA1 2BE, United Kingdom*
- ⁵² *University of Western Australia, Crawley, Western Australia 6009, Australia*
- ⁵³ *Department of Astrophysics/IMAPP, Radboud University Nijmegen, P.O. Box 9010, 6500 GL Nijmegen, The Netherlands*
- ⁵⁴ *Artemis, Université Côte d'Azur, CNRS, Observatoire Côte d'Azur, CS 34229, Nice cedex 4, France*
- ⁵⁵ *Institut de Physique de Rennes, CNRS, Université de Rennes 1, F-35042 Rennes, France*
- ⁵⁶ *Washington State University, Pullman, WA 99164, USA*
- ⁵⁷ *Università degli Studi di Urbino "Carlo Bo," I-61029 Urbino, Italy*
- ⁵⁸ *INFN, Sezione di Firenze, I-50019 Sesto Fiorentino, Firenze, Italy*
- ⁵⁹ *University of Oregon, Eugene, OR 97403, USA*
- ⁶⁰ *Laboratoire Kastler Brossel, UPMC-Sorbonne Universités, CNRS, ENS-PSL Research University, Collège de France, F-75005 Paris, France*
- ⁶¹ *Carleton College, Northfield, MN 55057, USA*
- ⁶² *Astronomical Observatory Warsaw University, 00-478 Warsaw, Poland*
- ⁶³ *VU University Amsterdam, 1081 HV Amsterdam, The Netherlands*
- ⁶⁴ *University of Maryland, College Park, MD 20742, USA*
- ⁶⁵ *Center for Relativistic Astrophysics and School of Physics, Georgia Institute of Technology, Atlanta, GA 30332, USA*
- ⁶⁶ *Laboratoire des Matériaux Avancés (LMA), CNRS/IN2P3, F-69622 Villeurbanne, France*
- ⁶⁷ *Université Claude Bernard Lyon 1, F-69622 Villeurbanne, France*
- ⁶⁸ *Università di Napoli "Federico II," Complesso Universitario di Monte S. Angelo, I-80126 Napoli, Italy*
- ⁶⁹ *NASA/Goddard Space Flight Center, Greenbelt, MD 20771, USA*
- ⁷⁰ *RESCEU, University of Tokyo, Tokyo, 113-0033, Japan.*
- ⁷¹ *Tsinghua University, Beijing 100084, China*
- ⁷² *Texas Tech University, Lubbock, TX 79409, USA*
- ⁷³ *National Tsing Hua University, Hsinchu City, 30013 Taiwan, Republic of China*
- ⁷⁴ *Charles Sturt University, Wagga Wagga, New South Wales 2678, Australia*
- ⁷⁵ *West Virginia University, Morgantown, WV 26506, USA*
- ⁷⁶ *University of Chicago, Chicago, IL 60637, USA*
- ⁷⁷ *Caltech CaRT, Pasadena, CA 91125, USA*
- ⁷⁸ *Korea Institute of Science and Technology Information, Daejeon 305-806, Korea*
- ⁷⁹ *Università di Roma "La Sapienza," I-00185 Roma, Italy*
- ⁸⁰ *University of Brussels, Brussels 1050, Belgium*
- ⁸¹ *Sonoma State University, Rohnert Park, CA 94928, USA*

- ⁸²Center for Interdisciplinary Exploration & Research in Astrophysics (CIERA),
Northwestern University, Evanston, IL 60208, USA
- ⁸³University of Minnesota, Minneapolis, MN 55455, USA
- ⁸⁴The University of Melbourne, Parkville, Victoria 3010, Australia
- ⁸⁵Institute for Plasma Research, Bhat, Gandhinagar 382428, India
- ⁸⁶The University of Sheffield, Sheffield S10 2TN, United Kingdom
- ⁸⁷The University of Texas Rio Grande Valley, Brownsville, TX 78520, USA
- ⁸⁸Università di Trento, Dipartimento di Fisica, I-38123 Povo, Trento, Italy
- ⁸⁹INFN, Trento Institute for Fundamental Physics and Applications, I-38123 Povo, Trento, Italy
- ⁹⁰The Pennsylvania State University, University Park, PA 16802, USA
- ⁹¹Cardiff University, Cardiff CF24 3AA, United Kingdom
- ⁹²Montclair State University, Montclair, NJ 07043, USA
- ⁹³MTA Eötvös University, “Lendulet” Astrophysics Research Group, Budapest 1117, Hungary
- ⁹⁴National Astronomical Observatory of Japan, 2-21-1 Osawa, Mitaka, Tokyo 181-8588, Japan
- ⁹⁵School of Mathematics, University of Edinburgh, Edinburgh EH9 3FD, United Kingdom
- ⁹⁶Indian Institute of Technology, Gandhinagar Ahmedabad Gujarat 382424, India
- ⁹⁷University of Szeged, Dóm tér 9, Szeged 6720, Hungary
- ⁹⁸Embry-Riddle Aeronautical University, Prescott, AZ 86301, USA
- ⁹⁹Tata Institute of Fundamental Research, Mumbai 400005, India
- ¹⁰⁰INAF, Osservatorio Astronomico di Capodimonte, I-80131, Napoli, Italy
- ¹⁰¹University of Michigan, Ann Arbor, MI 48109, USA
- ¹⁰²Rochester Institute of Technology, Rochester, NY 14623, USA
- ¹⁰³NCSA, University of Illinois at Urbana-Champaign, Urbana, Illinois 61801, USA
- ¹⁰⁴Universitat de les Illes Balears, IAC3—IEEC, E-07122 Palma de Mallorca, Spain
- ¹⁰⁵University of Białystok, 15-424 Białystok, Poland
- ¹⁰⁶SUPA, University of Strathclyde, Glasgow G1 1XQ, United Kingdom
- ¹⁰⁷IISER-TVM, CET Campus, Trivandrum Kerala 695016, India
- ¹⁰⁸Canadian Institute for Theoretical Astrophysics,
University of Toronto, Toronto, Ontario M5S 3H8, Canada
- ¹⁰⁹Institute of Applied Physics, Nizhny Novgorod, 603950, Russia
- ¹¹⁰Pusan National University, Busan 609-735, Korea
- ¹¹¹Hanyang University, Seoul 133-791, Korea
- ¹¹²University of Adelaide, Adelaide, South Australia 5005, Australia
- ¹¹³NCBJ, 05-400 Świerk-Otwock, Poland
- ¹¹⁴IM-PAN, 00-956 Warsaw, Poland
- ¹¹⁵Monash University, Victoria 3800, Australia
- ¹¹⁶Seoul National University, Seoul 151-742, Korea
- ¹¹⁷The Chinese University of Hong Kong, Shatin, NT, Hong Kong SAR, China
- ¹¹⁸University of Alabama in Huntsville, Huntsville, AL 35899, USA
- ¹¹⁹University of Massachusetts-Amherst, Amherst, MA 01003, USA
- ¹²⁰ESPCI, CNRS, F-75005 Paris, France
- ¹²¹Università di Camerino, Dipartimento di Fisica, I-62032 Camerino, Italy
- ¹²²Southern University and A&M College, Baton Rouge, LA 70813, USA
- ¹²³College of William and Mary, Williamsburg, VA 23187, USA
- ¹²⁴Instituto de Física Teórica, University Estadual Paulista/ICTP South
American Institute for Fundamental Research, São Paulo SP 01140-070, Brazil
- ¹²⁵University of Cambridge, Cambridge CB2 1TN, United Kingdom
- ¹²⁶IISER-Kolkata, Mohanpur, West Bengal 741252, India
- ¹²⁷Rutherford Appleton Laboratory, HSIC, Chilton, Didcot, Oxon OX11 0QX, United Kingdom
- ¹²⁸Whitman College, 345 Boyer Avenue, Walla Walla, WA 99362 USA
- ¹²⁹National Institute for Mathematical Sciences, Daejeon 305-390, Korea
- ¹³⁰Université de Lyon, F-69361 Lyon, France
- ¹³¹Hobart and William Smith Colleges, Geneva, NY 14456, USA
- ¹³²Janusz Gil Institute of Astronomy, University of Zielona Góra, 65-265 Zielona Góra, Poland
- ¹³³King’s College London, University of London, London WC2R 2LS, United Kingdom
- ¹³⁴Andrews University, Berrien Springs, MI 49104, USA
- ¹³⁵Università di Siena, I-53100 Siena, Italy
- ¹³⁶Trinity University, San Antonio, TX 78212, USA
- ¹³⁷University of Washington, Seattle, WA 98195, USA
- ¹³⁸Kenyon College, Gambier, OH 43022, USA
- ¹³⁹Abilene Christian University, Abilene, TX 79699, USA
- ¹⁴⁰Cornell University, Ithaca, NY 14853, USA
- ¹⁴¹Theoretical Physics Institute, University of Jena, 07743 Jena, Germany
- ¹⁴²Caltech JPL, Pasadena, CA 91109, USA